Surface Behaviors and Biocompatibility of Ti-40Nb-xTa Alloys Coated with Hydroxyapatite and Zirconium by Sputtering Methods

조선대학교 대학원

치의생명공학과

임 병 석

Surface Behaviors and Biocompatibility of Ti-40Nb-xTa Alloys Coated with Hydroxyapatite and Zirconium by Sputtering Methods

스퍼터링법을 이용하여 하이드록시아파타이트와 지르코늄 코팅된 Ti-40Nb-xTa 합금의 표면거동과 생체적합성

2023년 2월 24일

조선대학교 대학원

치의생명공학과

임　병　석

Surface Behaviors and Biocompatibility of Ti-40Nb-xTa Alloys Coated with Hydroxyapatite and Zirconium by Sputtering Methods

지 도 교 수   최 한 철

이 논문을 공학석사학위신청 논문으로 제출함

2022년 10월

조선대학교 대학원

치의생명공학과

임   병   석

임병석의 석사학위논문을 인준함

위 원 장   조선대학교   교 수   김 병 훈 (인)

위   원   조선대학교   교 수   안 상 건 (인)

위   원   조선대학교   교 수   최 한 철 (인)

2022년 12월

조 선 대 학 교 대 학 원

CONTENTS

LIST OF TABLES

LIST OF FIGURES

국 문 초 록

스퍼터링법을 이용하여 하이드록시아파타이트와 지르코늄 코팅된 Ti-40Nb-xTa 합금의 표면거동과 생체적합성

임 병 석

지도교수 : 최 한 철, 공학/치의학 박사

치의생명공학과

조선대학교 대학원

Ti-6Al-4V 합금은 우수한 내식성과 높은 기계적 성질로 임플란트 및 보철물 같은 생체 소재 응용 분야에서 광범위하게 사용되는 합금이다. 하지만 인체에 해로운 영향을 줄 수 있는 알루미늄 및 바나듐 이온을 방출할 수 있기 때문에 본 연구에서는 기존에 사용되는 Ti-6Al-4V 합금을 대체하기 위하여 순수한 Ti에 무독성이고 β형 안정화 원소인 Nb와 Ta를 첨가하여 새로운 3원계 합금(Ti-40Nb-xTa)을 제조하였다.

제조된 Ti-40Nb-xTa 합금에 생체적합성을 향상시키기 위하여 플라즈마 전해 산화(PEO) 처리로 마이크로 크기의 거칠기를 가진 여러가지 산화막을 형성하였다. 그 위에 Zr-HA 코팅을 RF-마그네트론 스퍼터링 처리한 후 표면 특성과 생체적합성을 관찰하였다.

Ti-40Nb-xTa 합금은 Ar 분위기의 진공 아크 용해로에서 순수한 Ti에 β형 원소인 Nb를 40 wt.% 첨가하고 Ta 함량을 x = 0, 3, 7, 15 wt.% 로 변화시켜 제조하였다. 그리고 균질화를 위해 1050℃에서 1시간 동안 유지한 후, 얼음물에서 급랭시켰다.

PEO 처리는 2000 grit까지 샌드페이퍼로 연마한 후, Ca 및 P 원소를 도핑하기 위하여 0.15M calcium acetate monohydrate + 0.02M calcium glycerophosphate의 전해질에서 수행하였으며 시편을 양극으로 탄소봉을 음극으로 세팅한 후, DC 전원(Keysight Co. Ltd., USA)을 사용하여 280V의 전압을 3분동안 인가하였다. 그 후 RF-마그네트론 스퍼터링을 이용하여 Ar 분위기에서 Zr-HA을 코팅하였다. Ti-40Nb-xTa 합금의 코팅된 표면은 광학현미경, 주사전자현미경, EDS, XRF 및 X선 회절분석기로 분석하였고 기계적인 특성은 나노인덴테이션 시험기를 통해 경도와 탄성계수를 분석하였으며, AFM을 통해 표면거칠기를 측정하였다. 동전위 분극실험으로 내식성을 평가하였으며 젖음성(wettability test) 시험, SBF 형성 시험으로 생체적합성을 평

가하여 다음과 같은 결과를 얻었다.

1. Ti-40Nb-xTa 합금에서 Ta 함량이 증가함에 따라 마르텐사이트 조직이 감소하였다. 마르텐사이트 결정구조인 α"상의 피크는 주로 Ta 함량이 증가함에 따라 감소하는 반면, 등축 구조를 갖는 β상의 피크는 증가하였다. 또한 Ta의 함량이 증가함에 따라 압입경도 및 탄성계수도 감소하였다.

2. Ti-40Nb-xTa 합금의 Ca와 P이온을 함유한 전해질에 PEO 공정을 수행한 결과, 표면의 전체적인 형상은 다공성이었고 불규칙한 형태의 기공이 관찰되었다. Ta 함량이 증가함에 따라 합금 표면 기공률, 기공 크기, 산화막 두께는 증가하였으나 기공의 수는 감소하였다. 또한 PEO 공정 후 합금 표면에 anatase, rutile, Nb_2O_5, Ta_2O_5, HA 등의 결정상이 나타났다.

3. Ca 및 P 이온을 포함하는 전해질에서 PEO 처리 후 스퍼터링을 통해 Zr-HA로 코팅한 Ti-40Nb-xTa 합금의 표면 형상은 다르지 않았지만, 고배율의 FE-SEM과 EDS 분석 결과 Zr 및 HA 이온이 표면에서 관찰 및 검출되었다. 스퍼터링 공정 후 XRD 분석 결과 표면에 anatase, rutile, Nb_2O_5, Ta_2O_5, HA 등의 결정상이 나타났으며, HA 피크가 강해지고 Zr 피크가 새롭게 검출되었다.

4. PEO와 Zr-HA로 코팅된 Ti-Nb-xTa 합금 코팅의 접착력은 코팅 두께에 비례하여 Ta 함량이 증가함에 따라 증가하였다. 또한 코팅 전과 후 모두 Ta 함량이 증가하면 부식전위가 증가하였다. 또한 Zr과 HA의 영향으로 코팅 후 부식 전위가 증가하고 전류 밀도가 감소하여 내식성이 크게 증가하였다.

5. PEO 표면처리 후 미세한 크기의 기공이 형성되어 거칠기가 벌크 합금에 비하여 크게 증가하였다. 이때, Ta의 함량이 증가할수록 기공 크기가 커지고 표면 거칠기가 증가하는 경향을 보였다. Zr-HA 코팅은 박막 형태로 코팅되어 스퍼터링 후 표면 거칠기의 큰 차이는 없었다.

6. 표면 처리된 Ti-40Nb-xTa 합금의 젖음성을 측정한 결과, 접촉각은 벌크 합금에 비해 전체적으로 감소하였으며, Ta 함량이 증가하고 Zr과 HA가 코팅된 경우 접촉각이 감소하였다.

7. 수산화인회석의 성장과 석출은 산화막 표면에 전체적으로 형성하였고, 주로 기공 주변에 핵이 성장을 시작하여 시간이 지남에 따라 성장하였다. PEO 공정 중 산화막에 HA 입자의 형성과 Zr-HA 코팅이 수산화인회석 형성에 도움이 되었다.

본 연구에서 개발된 Ti-40Nb-xTa 합금은 무독성이며 기존 임플란트 재료로 사용되던 Ti 합금에 비해 탄성계수가 낮다. 또한 PEO 공정을 통해 다공성 산화막을 형성함으로써 높은 표면 거칠기와 넓은 표면적을 얻을 수 있으며 이때 형성된 산화막에 기능성 물질을 도핑하면 생체적합성을 더 향상시킬 수 있다. 따라서 표면 개질 및 Zr-HA 코팅된 Ti-40Nb-xTa 합금은 임플란트 식립 후 뼈와 임플란트 사이의 빠른 골 융합을 통해 치유 시간을 단축시킬 것으로 생각된다.

Ⅰ. INTRODUCTION

An implant is an artificial fixture placed in or on the jawbone to support a prosthesis to restore a missing tooth. Titanium alloys possess good fatigue characteristics, moderate corrosion resistance, strong wear resistance, high strength, and biocompatibility, which makes them primary design choices for a variety of clinical applications, including dental implants, bone plates, and screws [1,2]. A common material utilized in biological applications is the Ti-6Al-4V alloy, which is categorized as a Grade 5 alloy and has alpha and beta phases [2,3]. Because Ti-6Al-4V alloy has insufficient osseointegration, its effect on aluminum and vanadium elements may cause toxic reactions in adjacent cells or lead to implant failure [3,4]. And Ti-6Al-4V alloy has a high elastic modulus (110 GPa) compared to cortical bone (20 ~ 30 GPa) [5,6].

To solve this problem, new β-Ti alloy research using β-stabilizer including such as Mo, Sn, Nb, Ta, Zr, Cr, and Fe, which are non-toxic and has a relatively low elastic modulus, is attracting attention [7]. The mechanical advantages of β-titanium alloys over current α+β titanium alloys used in biomedical applications include better wear resistance, high elasticity, and superior cold and high-temperature formability [8]. The low elastic modulus allows bone tissue to easily grow on a stable TiO_2 layer, improving osseointegration [9,10]. Nb and Ta are among the most effective titanium β-stabilizers to reduce the elastic modulus, and adding small amounts of Ta to Ti creates a Ta_2O_5 layer on the surface of the alloy to improve corrosion resistance and biocompatibility [10]. It is reported that titanium-based implants are difficult to form direct osseointegration with natural bone due to the bioinert nature of Ti [11]. The biocompatibility and adhesion of alloys have thus been improved by the introduction of several surface modification techniques. Surface of implant can be coated using techniques including electrophoretic deposition, sol-gel process, plasma spraying, micro-arc oxidation (MAO), and RF-magnetron sputtering to enhance their chemical and biological properties [12].

By using direct current or alternating current polarization, plasma electrolytic oxidation (PEO), also known as micro-arc oxidation (MAO), creates a plasma

micro-discharge on the electrode surface to produce high temperatures and high pressures for surface treatment [13]. PEO is an environmentally friendly and simple coating technology that promotes osseointegration and shortens the rehabilitation time by producing a bioactive oxide layer on the titanium alloy [14]. In addition, PEO has the advantage of uniformly coating the porous and irregularly shaped TiO_2 layer, and excellent cell adhesion and coating adhesion [14,15]. When PEO is carried out in an electrolyte containing Ca^{2+} and PO_4^{3-} ions, the coating material is a ceramic with calcium phosphate and hydroxyapatite (HA) as its main components. Because of its structural similarity to bone, $HA[Ca_{10}(PO_4)_6(OH)_2]$ is a very promising ceramic material with excellent bioactivity [16,17].

PVD magnetron sputtering is a high-speed vacuum coating technique that uses ions and atoms from a source target in an inert gas to deposit a film on the surface of a metallic material [12]. Target materials for magnetron sputtering range from pure metals, which can be powered by DC power, to semiconductors and insulators, which need RF power or pulsed DC [18]. Radiofrequency (RF) magnetron sputtering, which can form hard, dense, and uniform coatings with thicknesses 1 μm and that are homogeneous in both structure and composition, is an effective deposition technique for HA and mineral components in bones [15]. The RF/DC simultaneous application magnetron sputtering deposition method enables low-voltage sputtering, which reduces plasma damage, lowers discharge gas pressure, and reduces the scattering of thin film atoms [19]. Zirconium (Zr) is a non-toxic element when used as an implant material. It does not cause health problems in the long term and has high corrosion resistance. In addition, because thin layers of polycrystalline zirconium films have low thermal conductivity and resilience to thermal shock, zirconium is also often used for refractory applications [20,21].

In this study, Ti-40Nb-xTa, a ternary alloy containing Nb and Ta, which is non-toxic and has a low elastic modulus of Ti, was developed. After that, the surface of alloys was covered with a porous oxide layer comprising HA and Zr using a variety of techniques, and numerous experiments were performed to look into the surface of layer properties and biocompatibility. Surface properties were analyzed using a field emission scanning electron microscope (FE-SEM), optical microscope (OM), energy dispersive

X-ray spectrometer (EDS), X-ray diffraction (XRD), and atomic force microscope (AFM). A nano-indentation was used to measure the mechanical properties of hardness and elastic modulus, and an AFM was used to measure roughness. Corrosion resistance was evaluated by a potentiodynamic test, and biocompatibility was evaluated by a wettability test and SBF formation.

Ⅱ. BACKGROUND

Ⅱ. 1. Bio-metallic materials

Bio-metallic materials are artificial structures designed to naturally support biological tissues. Outstanding mechanical qualities, osseointegration, strong corrosion resistance, and exceptional wear resistance are the main requirements for metals as biomaterials. This means that components of implants are likely to be highly toxic and should not cause the human body to get inflamed or react allergically [22]. In particular, for use as biomaterials, toxicity and elastic modulus must be taken into account to avoid ion release and inflammatory responses and the "stress shielding" effect of metals in the body [23].

Figure 1 shows the results of a study on the biocompatibility of common metals and alloys. Figure 1 (a) shows Fe, Co, Bi, Ag, Sr, Mg, V, Cu, Zn, Cd, and Hg are highly cytotoxic elements, and Zr, Nb, Ta, Pt, and Ti have excellent biocompatibility. Figure 2 (b) shows the relationship between polarization resistance and biocompatibility. Co, Cu, Ni, and V showed cytotoxicity, and in the case of Co-Cr alloy, Ag, Au, Mo, Al, and Fe, the capsule-type tissue response was demonstrated. and Pt, Ta, Nb, Ti, and Zr showed excellent biocompatibility according to the degree of polarization resistance [23]. Among them, Mo, Nb, and Ti show excellent biocompatibility due to their high cell viability compared to other metals. Based on these results, Ti-based alloys were prepared and cytotoxicity was evaluated. As a result, the cell viability was increased in the Ti-based alloy compared to pure titanium, and the cell viability was the highest in the Ti-Nb alloy [24].
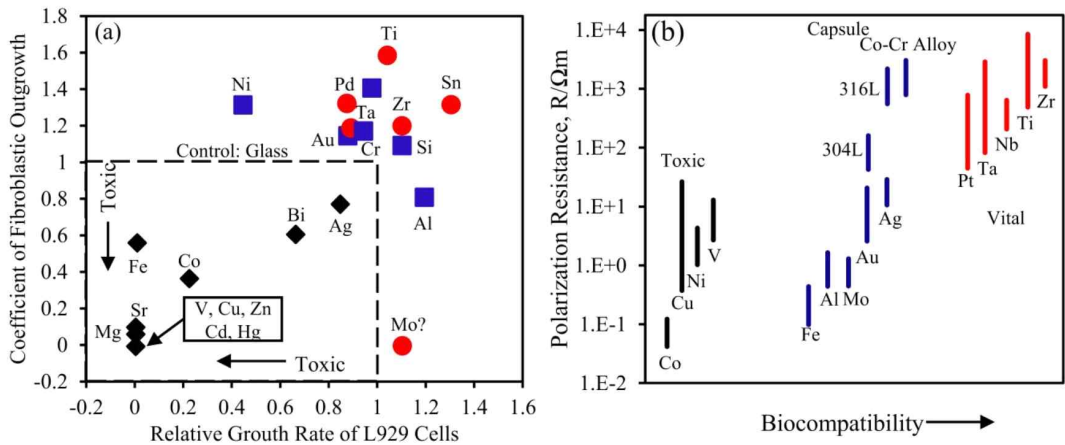
Fig. 1. Common metals and biocompatibility of alloys: (a) toxicity and (b) comparing biocompatibility and polarization resistance [24].

Ⅱ. 2. Titanium alloys

One of the most widely distributed and ninth most abundant metals on the earth, titanium is a metal with a silvery-white sheen. With an atomic weight of 47.9 and an atomic number of 22, it was discovered as one among the transition elements of groups IV and 4 of the Mendeleev periodic table in the late 18th century, although smelting did not begin until the early 20th century. Therefore, despite its abundant reserves, it is an expensive metal that is difficult to extract, smelt, and process due to its strong durability. Today, due to its high strength and lightweight, it is widely used in the aerospace industry, dental implants, and orthopedic materials. The basic physical properties of titanium are shown in Table 1 [25].

The four main categories of titanium's microstructure are pure α, near- α, α+β, and β phase alloys. Ti alloying elements can be divided into three major groupings according to the four criteria mentioned: neutrals, α-stabilizers, and β-stabilizers. Figures 1 and 2 show how Ti alloys go through several phases. Essentially, Ti changes structurally at 882°C in pure Ti. The term "transformation temperature, T_β," is used to describe this temperature. Below this temperature, commercially pure Ti (cp-Ti) has a hexagonal close-packed (hcp), or α–phase, structure. Above 882°C, a phase shift occurs, causing hcp to progressively transform into a body-centered cubic (bcc) structure. Generally, this transformation produces a two-phase field with both α and β phases, but when the amount of β-stabilizer increases, only the β phase slowly emerges [26]. The transformation temperature of a titanium alloy from α to β depends on the nature and concentration of the element when the element is added to titanium. Stabilizers are alloying components like Al, O, N, and C that tend to stabilize the α phase. These α stabilizing elements increase the β transformation temperature. β Stabilizers are substances like Fe, MO, Nb, Ta, V, and Cr that keep the β phase stable. These β stabilizing elements reduce the β transformation temperature. Figure 3 shows the α (a) and β (b) crystal structures of titanium and the titanium phase transformation according to alloying elements [27].

According   to   ASTM (American   Society   for   Testing   and   Materials),   in   the

microstructure of titanium alloys, alloys containing only α-stabilizing elements and consisting only of α-phases and containing 1 ~ 2% β-stabilizing elements and about 5 ~ 10% β-phases The alloy is called an α alloy. Alloys that contain a greater amount of β-stabilizing elements and produce 10 ~ 30% of the β-phase in the microstructure are called α+β alloys, and alloys with a greater amount of β-stabilizing elements are called α+β alloys, and by rapid cooling, the β-phase is brought to room temperature. It can be maintained at and is said to be a metastable β alloy. These alloys tend to decompose into α+β alloys upon age hardening, and most titanium alloys used in biomedical applications have α+β or metastable β phases. Table 2 shows biomedical-grade titanium alloys according to ASTM. Ti-6Al-4V and pure titanium (cp-Ti) are mostly employed as orthopedic and dental materials. [27].

Table 1. Summary of the unalloyed titanium's physical characteristics [25]

Atomic number	22
Density at room temperature, g/cm^3	4.5
Boiling point, ℃	3.287
Melting point, ℃	1.668
Relative abundance in the crust of the Earth, %	0.44
Heat of sublimation latent, J/mol	464.7
Heat of fusion latent, kJ/mol	20.9
Heat of vaporization latent, kJ/mol	397.8
body centered cubic ⇆ Hexagonal close-packed	
Lattice constants of α-Ti at room temperature, nm	a = 0.2951
	c = 0.4679
Atomic weight (g/mol)	47.88
Atomic radius of the crystal's sixth coordination, nm	0.145
Phase transformation temperature, ℃	882
Coefficient of linear expansion at 25℃, K^{-1}	8.5 × 10^{-6}
Heat of transformation, kJ/mol	3.685
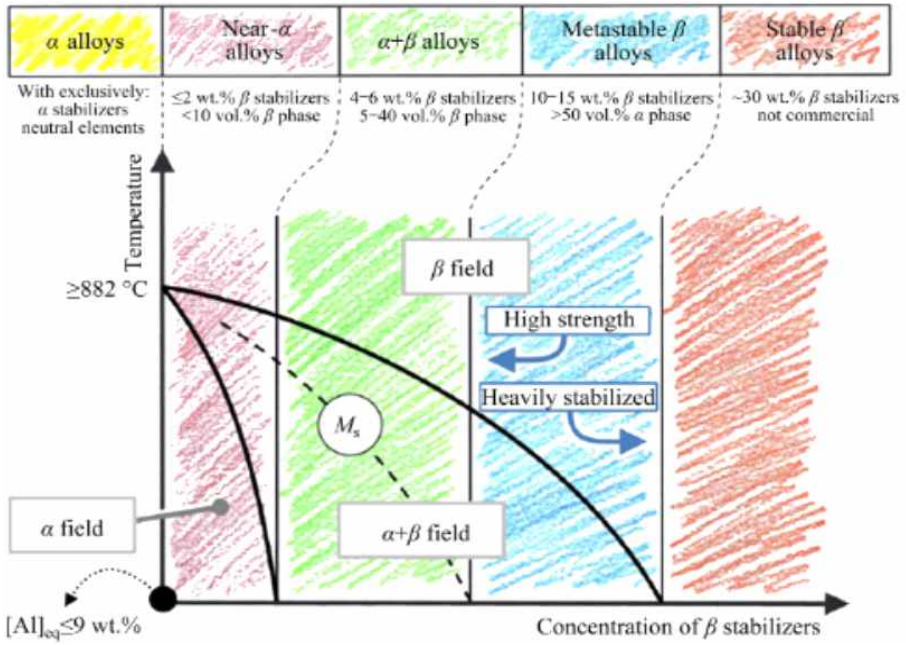
Fig. 2. Classification of titanium alloys [26].
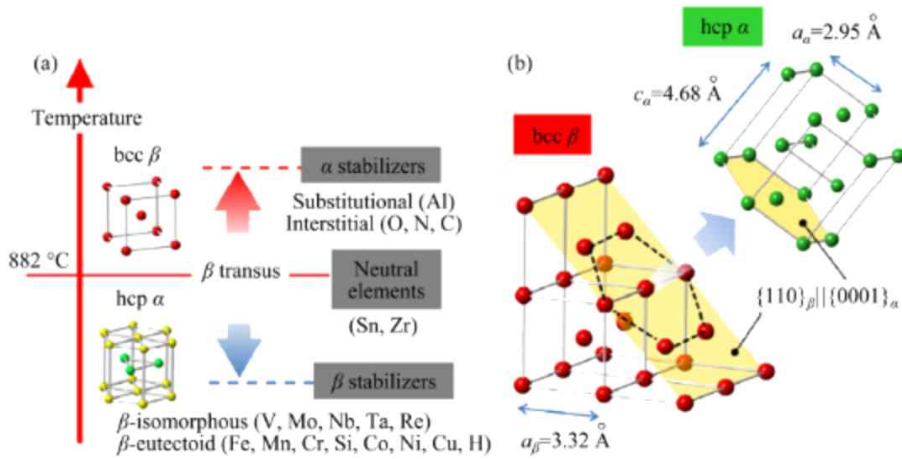
Fig. 3. Ti-based alloys' crystal structures have changed as a result of the alloying components (a), and correspondence in the lattice between hcp-α and bcc-β structure (b) The lattice parameters match those of pure titanium at 900°C and temperature [26].
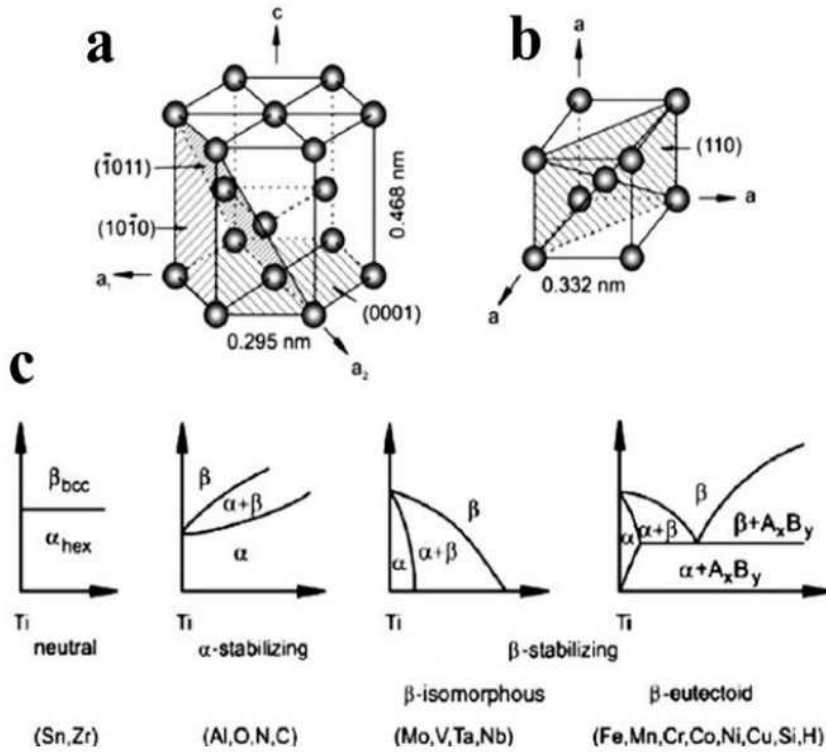
Fig. 4. Structures of alpha (a) and beta (b) of titanium and the several forms of phase diagrams for titanium that depend on the alloying elements [27].

Table 2. Biomedical grade titanium alloys [27]

Titanium Alloys	Standard	Alloy Type
Initial generation (1950 ~ 1990)		
Connercially pure Ti (cp Grade 1-4)	ASTM 1341	α
Ti-5Al-2.5Fe	-	α + β
Ti-6Al-4V ELI wrought	ASTM F136	α + β
Ti-6Al-7Nb wrought	ASTM F1295	α + β
Ti-6Al-4V ELI standard grade	ASTM F1472	α + β
Subsequent generation (1990 ~ till date)		
Ti-13Nb-13Zr wrought	ASTM F1713	Metastable β
Ti-35Nb-5Ta-7Zr-0.4O (TNZTO)	-	β
Ti-15Mo-5Zr-3Al	-	β
Ti-35Nb-7Zr-5Ta (TMZT)	-	β
Ti-29Nb-13Ta-4.6Zr	-	β
Ti-12Mo-6Zr-2Fe (TMZF)	ASTM F1813	β
Ti-Mo	ASTM F2066	β

Ⅱ. 3. Titanium alloy as a bio-metallic materials

Dental implants can be created using alloys including a variety of metals. Great mechanical strength, corrosion resistance, and wear resistance are characteristics of titanium and titanium alloys. On the titanium's surface, they also generate a stable oxide layer (Ti matrix). As a bone transplant material for implants, it has a high biocompatibility and is extensively utilized [1,28]. Due to its strong corrosion resistance and outstanding biocompatibility, Ti-6Al-4V alloy is especially utilized in the biomedical disciplines even though it was initially created for aerospace uses [27]. However, the Ti-6Al-4V alloy's influence on the aluminum and vanadium elements may create a toxic response in nearby cells or result in implant failure since the alloy's osseointegration is insufficient [29]. Additionally, titanium accumulation in tissues near the implant would indicate metal leakage and degradation in vivo. Additionally, upon implantation, these metal implants tendten to become loose and potentially separate from the surrounding tissues [30]. To solve this problem, research on new β-Ti alloys using β-stabilizing elements is attracting attention [7]. The β-type element reduces the titanium alloy's modulus, eliminating the stress shielding effect brought on by the implant's and the bone's different modulus. Young's modulus values for various alloy types are illustrated in Figure 5, with the β-titanium alloy having a lower Young's modulus value than the current α+β titanium alloy [31].

Cells in contact with the implant have different growth and differentiation depending on the surface roughness, which is important for success after implant placement [29]. In particular, bone adhesion needs to be improved for therapeutic usage in individuals with weak bones [32]. Additionally, research is being done to increase osteoblast adhesion, proliferation, and bone formation using different surface treatments on the implant in order to prolong implant life through strong chemical bonding between the bone tissue and implant after implantation [33].
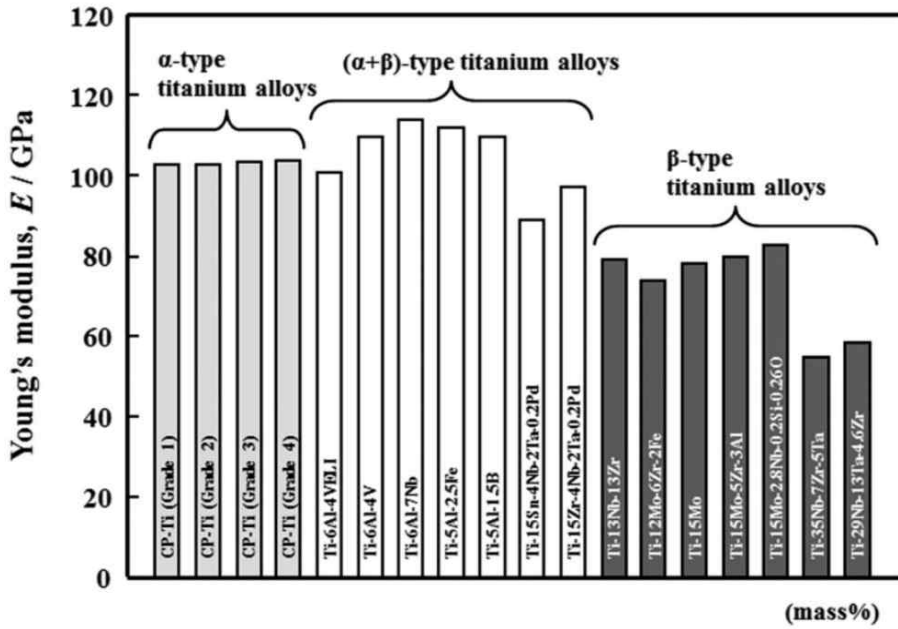
Fig. 5. Young's modulus of typical titanium alloys of the α-type, (α+β)-type, and β -type [31].

Ⅱ. 4. Ti-40Nb-xTa alloys

Ⅱ. 4. 1. Ti-Nb alloy

Niobium (Nb) is non-toxic and is known to change α-Ti to β-Ti when used as a β-type element in titanium alloys. As the Nb content added to the alloy increases, the alloy changes from a two-phase (α″+β) to a single-phase (β), and the average grain size and tensile strength of the β phase decrease. Ti-Nb has been reported as a shape-memory alloy, and a high degree of structural porosity has been reported to reduce the mechanical properties of the alloy. Numerous studies have been done on the manufacturing of Ti-Nb implants because titanium alloys with Nb components have good corrosion resistance [34,35].

Ⅱ. 4. 2. Ti-Ta alloy

Tantalum, a β-type element with exceptional corrosion resistance, has gained attention recently as a useful alloying component for titanium alloys. Ta also possesses chemical characteristics akin to those of glass and is resistant to practically all acids, with the exception of strong HF [36]. Ti-Ta binary alloys are reported to have greater corrosion resistance than pure titanium in reducing acids and are lighter and less expensive than pure tantalum [37]. In addition, Ti-Ta alloys are reported to have a lower Young's modulus than the implant materials now in use. The non-toxicity and corrosion resistance of the alloy constituents are very crucial in terms of the use of Ti-Ta alloy in medicine. This is because TiO_2 and Ta_2O_5 oxides form spontaneously, which inhibits the dissolution of Ti and Ta into ions in aggressive body fluids [38].

Ⅱ. 4. 3. Ti-Nb-Ta alloys

Tantalum (Ta) and niobium (Nb) are β-stabilizing elements of Ti and have low toxicity, and can inhibit the dissolution and release of metal ions by forming a self-passivating film. Additionally, it is useful for biocompatibility because it is highly stable over a broad pH range. This is because, like Ti, Nb and Ta form a stable oxide film with Nb_2O_5 and Ta_2O_5 when exposed to an oxygen atmosphere and have excellent corrosion resistance [36]. The widespread use of Nb and Ta is difficult despite their high melting points. However, titanium (Ti) can help lower the melting points of Nb-Ta alloys. Nb and Ta are strong β-stabilizing elements, contributing to lowering the elastic modulus of Ti alloy, reducing the "stress shielding effect" in clinical applications, thereby reducing bone resorption and implant failure [39].

Ⅱ. 5. Surface treatment of titanium alloy

Ⅱ. 5. 1. Plasma electrolytic oxidation (PEO)

By using direct current or alternating current polarization, plasma electrolytic oxidation (PEO), also known as micro-arc oxidation (MAO), creates a plasma micro-discharge on the electrode surface to produce high temperatures and high pressures for surface treatment [13]. PEO can include ions such as calcium (Ca) and phosphorus (P) in the process of preparing the oxide layer and can have excellent biocompatibility and improve mechanical properties by changing the crystallinity and shape of the coating [40]. The PEO approach increases the bonding strength by covering biologically active substrates with a variety of shapes, and it can be used in other ways to provide the best results. The manufacture of complex types such as HA, HA-TiO$_2$, Ca, and PO$_4$ on titanium alloys can form a coating layer relatively easily, as well as improve the chemical, physical, and electrochemical properties [36]. In particular, it is an economical and convenient technology that is easy to process by inducing bone bonding by adding Ca and PO$_4$ ions to the electrolyte. Additionally, PEO has the benefit of allowing the process to be controlled in a variety of ways, including electrolyte composition, voltage, current density, and time [40].

When plasma electrolytic oxidation (PEO) is taking place, the anode's primary reactions are [36]:

(1) $Ti \rightarrow Ti^{2+} + 4e^-$

(2) $2H_2O \rightarrow 2O^{2-} + 4H^+$

(3) $2H_2O \rightarrow O_2(gas) + 4H^+ + 4e^-$

(4) $Ti^{2+} + 2O^{2-} \rightarrow TiO_2 + 2e^-$
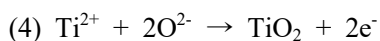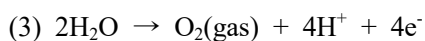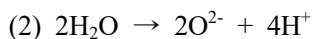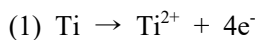
The PEO process results in the synthesis of titanium oxide and HA product when Ca and P are added to the electrolyte [41].

(1) $Ti \rightarrow Ti^{2+} + 4e^-$

(2) $Ti^{4+} + 2OH^- \rightarrow TiO_2 + 2H^+$

(3) $Ca^{2+} + OH^- \rightarrow Ca^- + H^+$

(4) $3Ca^{2+} + 2PO_4^{3-} \rightarrow Ca(PO_4)_2$

(5) $10Ca^{2+} + 6PO_4^{3-} + 2H_2O \rightarrow Ca_{10}(PO_4)_6(OH)_2 + 2H^+$
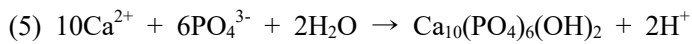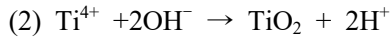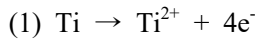
The electrode reaction during electrolysis in the electrolyte is shown in Figure 6 [13]. An oxidation reaction takes place at the anode and a reduction reaction takes place at the cathode when a voltage is applied after creating a circuit in the electrolyte consisting of an anode and a cathode. That is, oxygen gas is generated on the surface of the anode or an oxidation reaction of the metal occurs. At the cathode, hydrogen gas is generated or a reduction reaction occurs.
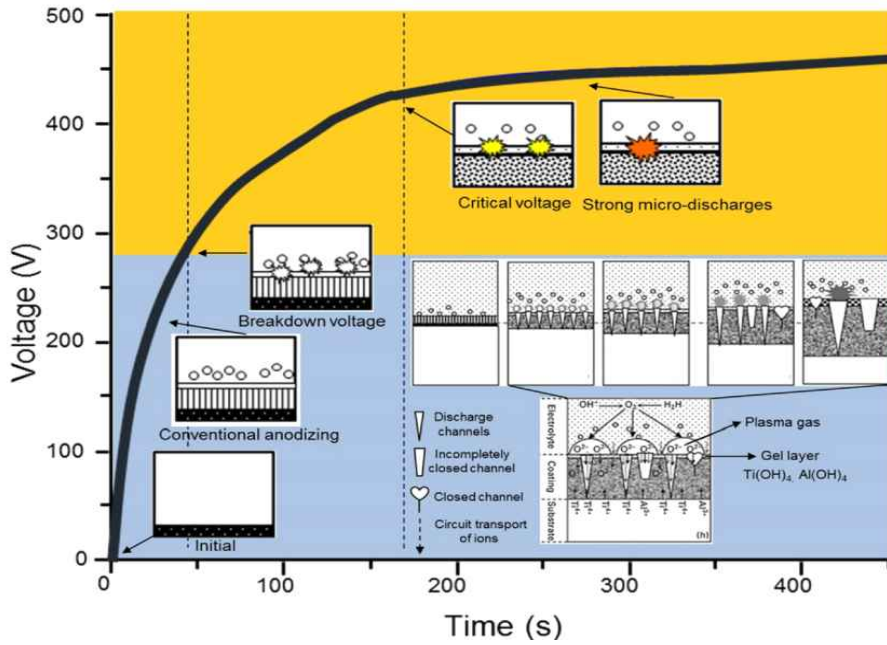
Fig. 6. Schematic illustration of PEO treatment showing the formation of a coating layer and the sparking phenomenon as a function of time [13].

Ⅱ. 5. 2. RF-magnetron sputtering

The most popular surface engineering treatment approach at the moment is magnetron sputtering, which coats a thin film on the surface of a metal material using one of the physical vapor deposition techniques. In addition, a permanent magnet is mounted at the cathode to apply a magnetic field in a direction parallel to the target surface. A target equipped with such a permanent magnet is called a magnetron target. Among magnetron sputtering, RF-magnetron sputtering is similar to DC-sputtering, but various types of metals and alloys as conductors and ceramics as non-conductors can also be used as targets, so there is no restriction in target selection. In RF-magnetron sputtering, plasma is generated by the ionization of a low-pressure inert gas by an electric field. In the thin film on the substrate, positive ions in the plasma are accelerated to the target by the force of the electric field. The accelerated cations repel the cathode material from the target. Then, source atoms and molecules are emitted from the target surface and fly to the substrate to be deposited and grown. Films formed by sputtering are more uniform, have higher adhesion strength, and have smaller grain sizes than films formed by thermal evaporation. It is also a process that is carried out in a vacuum and inert gas atmosphere, making it easy to coat heat-sensitive targets [12,42]. Figure 7 is a schematic diagram of an RF-magnetron sputtering system [43].
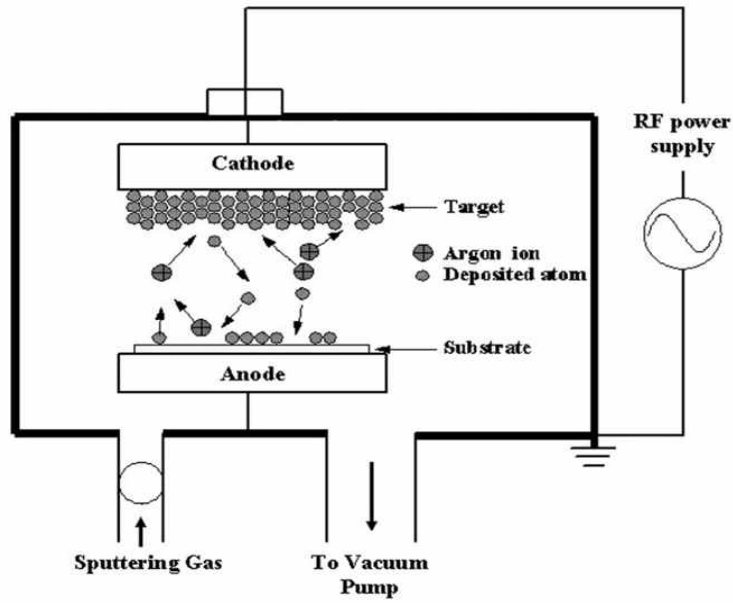
Fig. 7. The RF-magnetron sputtering system schematic drawing [43].

Ⅱ. 5. 2. 1. Hydroxyapatite (HA) properties and structure

Hydroxyapatite (HA) is chemically and structurally the most similar to the mineral components of human bones and teeth. The chemical formula of hydroxyapatite is $Ca_{10}(PO_4)_6(OH)_2$, and the lattice constant is 0.95 nm on the side and 0.68 nm on the c axis. The lattice structure of HA is shown in Figure 8, and when the crystal structure changes by substitution, various structures exist. Dicalcium phosphate dihydrate (DCPD), octacalcium phosphate (OCP), amorphous calcium phosphate (ACP), and Mg-substituted -tricalcium phosphate (b-TCMP), with stability and solubility, are the different types of calcium phosphate phosphate-basedc-axisbased on the structure of HA. and the material's characteristics, such as its reactivity, are also altered. It also improves the biological performance of synthetic bone graft materials by enabling cation and anion substitution. In calcium phosphate ceramics, the Ca/P ratio, solubility, and acidity are closely correlated.c-axis Acidity and solubility rise as the Ca/P ratio falls below 1.0 [44,45].
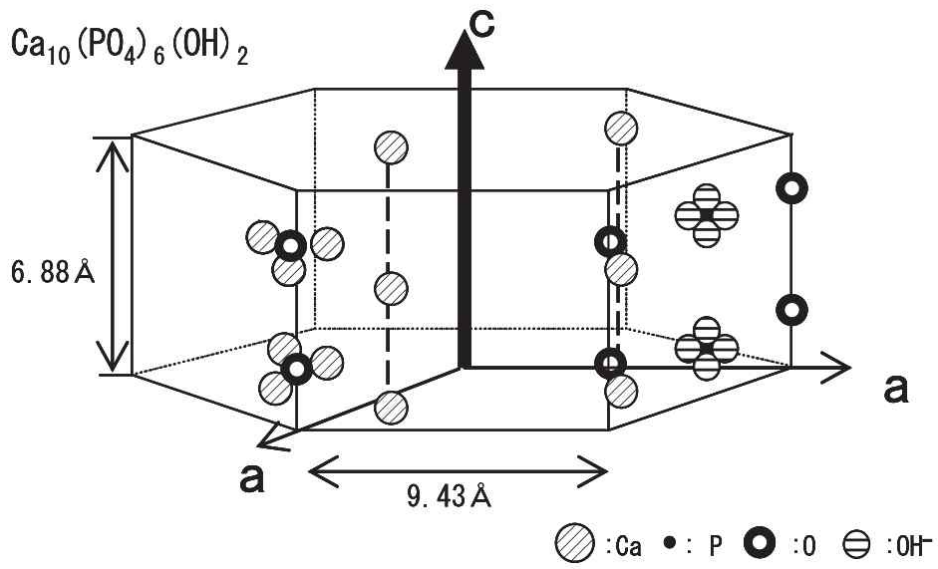
Fig. 8. Hydroxyapatite's crystal structure, $Ca_{10}(PO_4)_6(OH)_2$ [44].

Ⅱ. 5. 2. 2. Zirconium (Zr)

Zirconium (Zr) has a hexagonal dense crystal structure at room temperature and has high corrosion resistance and a low neutron absorption cross-section. This is due to ZrO_2 forming a passivation film. When the Zr element is added to titanium alloy, its mechanical properties can be improved, and zirconium (Zr) is a non-toxic element when used as an implant material and does not cause long-term health problems. In addition, osteoblasts on the surface of the Ti-Zr alloy show excellent bone formation ability due to the high expression of osteogenic genes and excellent initial osseointegration in vivo. There are many uses for thin multilayers of polycrystalline zirconium films, including the construction of metal superlattices. Because due to its poor heat conductivity and resilience to thermal shock, zirconium is frequently utilized in refractory applications [20,21]. Figure 9 is the crystal structure of cubic zirconium (c-ZrO_2) [46].
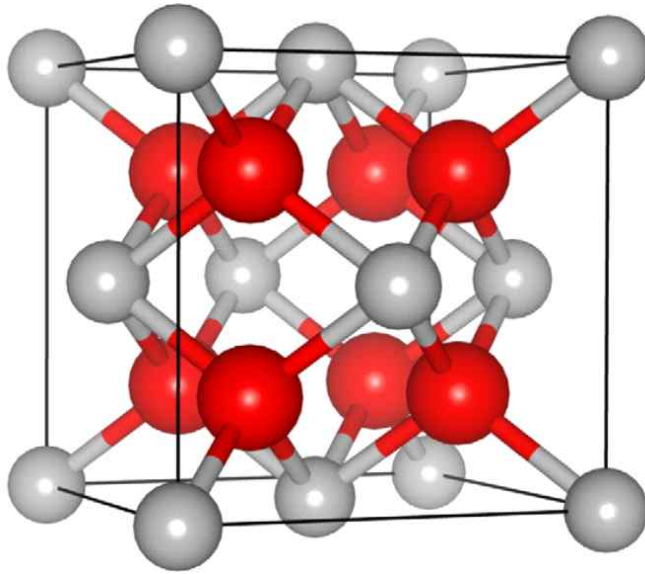
Fig. 9. Cubic zirconium's crystal structure (c-ZrO$_2$) [46].

Ⅲ. MATERIALS AND METHODS

Ⅲ. 1. Design of Ti-40Nb-xTa alloys

In this experiment, the Ta component was varied (x = 0, 3, 7, 15 wt%) to manufacture a Ti-40Nb-xTa alloy. The alloys were made from pellets of CP-Ti (G & S Titanium, Grade 4, 99.5% USA), Nb, and Ta (Kurt J. Lesker Company, 99.95% purity, USA). The alloy was produced in a vacuum arc melting furnace with a high-purity argon environment (Model MSTF-1650, MS Eng., Korea). Before manufacturing the designed alloy, CP-Ti was melted 5 times to remove residual oxygen in the furnace to minimize oxidation of the designed alloy. The designed alloy was homogenized by melting 10 times in the form of a button-type ingot and then a rod-type ingot using a tungsten (W) electrode. To further enhance chemical homogeneity, the manufactured rod-type alloy was heat-treated at 1050℃ for 1 hour in a high-temperature furnace (Model MSTF-1650, MS Eng., Korea). After that, it was cooled with water at 0℃. The heat-treated sample was cut into a 3 mm thick disc for the experiment using a high-speed diamond cutting machine (Accutom-5, Struers, Denmark) running at a speed of 2500 rpm. The sample was then gradually polished using 100-2000 SiC (silicon carbide) paper and 0.3 μm alumina powder until a mirror surface was visible (Al_2O_3). The polished sample was ultrasonically cleaned with ethyl alcohol and distilled water and then let to air dry. An X-ray diffractometer (XRD, X'pert Philips, Netherlands) was used to evaluate a 2θ section of 20˚ to 90˚, and the composition of the alloy was determined using an X-ray fluorescence analyzer (XRF, Analyzer Mde-Alloy, Analyzer Serial number-581331, OLYMPUS, Japan). In this paper, the name of the sample is named as follows; Ti-40Nb is 0Ta, Ti-40Nb-3Ta is 3Ta, Ti-40Nb-7Ta is 7Ta, and Ti-40Nb-15Ta is 15Ta, respectively.

Ⅲ. 2. Microstructure observation of alloys

The Ti-40Nb-xTa alloy was etched using Keller's solution (2 mL HF + 3 mL HCl + 5 mL HNO_3 + 190 mL H_2O). The etched sample was ultrasonically cleaned with ethyl alcohol and distilled water and then left to dry naturally. An optical microscope was used to analyze the microstructure of each alloy (OM, Olympus BX 60M, Japan).

Ⅲ. 3. Plasma electrolytic oxidation (PEO) treatment

The surface of the Ti-40-Nb-xTa alloy was polished with sandpaper to a 2000 grit level in order to get a sample ready for PEO treatment. After that, it was cleaned with distilled water, ethyl alcohol, and an ultrasonic cleaner. The cleaned sample served as the anode and a carbon rod served as the cathode under a DC power supply (Keysight Co. Ltd., USA). A voltage of 280V was used, and it was left on for three minutes. The sample was surface-treated, cleaned with ethyl alcohol and distilled water, and then dried to air dry. The electrolyte used for PEO treatment was prepared by mixing calcium glycerophosphate ($C_3H_7CaO_6P$) and calcium acetate monohydrate ($Ca(CH_3COO)_2 \cdot H_2O$), and Table 3 displays the electrolyte's concentration.

Table 3. The condition of plasma electrolytic oxidation

Experimental condition / Solutions	Composition of electrolyte		Applied voltage (V)	Applied time (min)
	Calcium acetate monohydrate (CH$_3$COO)$_2$·H$_2$O) (g/L)	Calcium glycerophosphate (C$_3$H$_7$CaO$_6$P) (g/L)		
Ca/P	0.15 M	0.02 M	280	3

Ⅲ. 4. RF-magnetron sputtering treatment

The schematic layout of the magnetron sputtering system (A-Tech System Co., Korea) utilized to coat Zr-HA on the Ti-40Nb-xTa alloy after PEO treatment is illustrated in Figure 9. After fixing the Zr (99.5%, teawon scientific co., Korea) target to one RF-magnetron sputtering gun and fixing an HA target to the opposite RF-magnetron sputtering gun, sputtering was performed. The target used in the magnetron sputtering experiment had a distance of 80 mm from the sample. To generate plasma, the initial vacuum level of the chamber was lowered to 1.0×10^{-3} Torr using a rotary pump, and then the vacuum level was lowered to 1.0×10^{-5} Torr using an oil diffusion pump. After the vacuum was lowered, 40 sccm of high-purity Ar gas was injected and maintained using a mass flow meter. During coating, the chamber pressure was maintained at 5.0×10^{-2} Torr, and the substrate temperature was set at 150℃ to increase ionic activity. Pre-sputtering was performed for 30 minutes to remove impurities from the target before coating. To deposit the Zr-HA thin film, the Zr target was deposited with a 100W RF-magnetron sputtering gun and the HA target with a 40W RF-magnetron sputtering gun for 30 minutes. The detailed experimental conditions of magnetron sputtering are shown in Table 4. Figure 10 shows an image of the magnetron sputtering process.
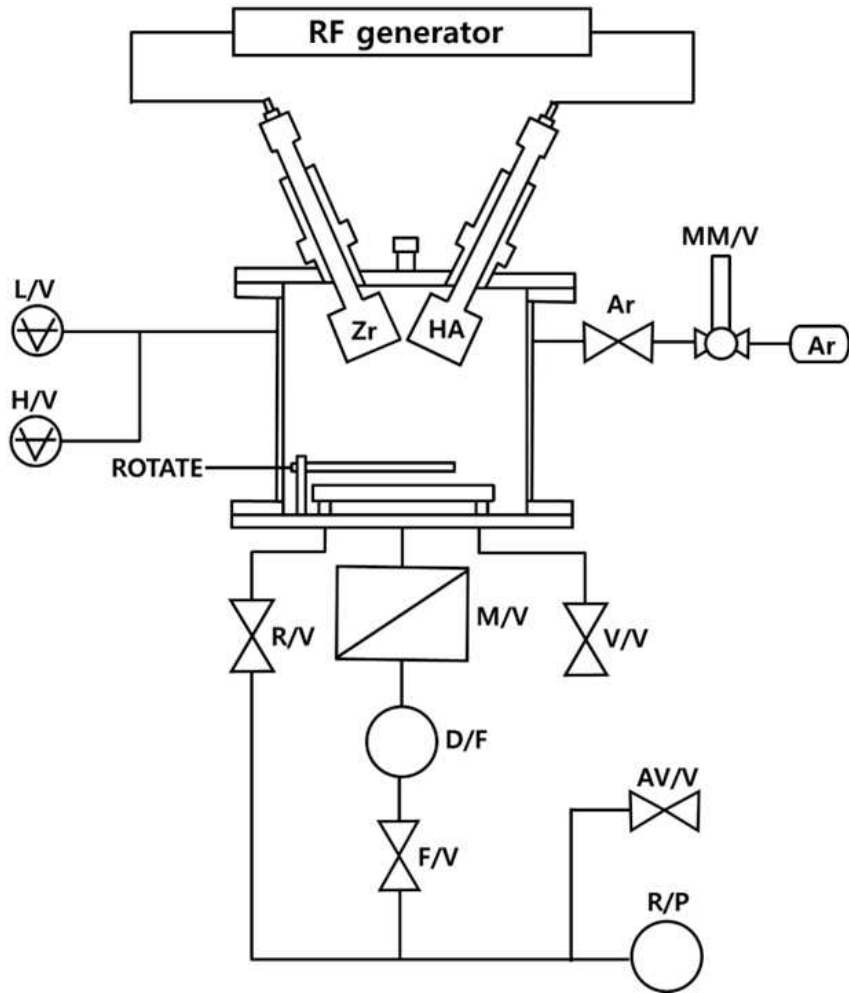
Fig. 10. Schematic diagram of magnetron sputtering system.

Table 4. Zr-HA target ingredient used in magnetron sputtering treatment

Coating condition	Zr-HA film
Target	Zr / HA (99.99%)
Gas	Ar (40 sccm)
Base pressure	1.0×10^{-3}
Working pressure	1.0×10^{-5}
Operation temperature	150℃
Pre-sputtering	30 min
Deposition time	30 min
Power supply	100 W / 40 W
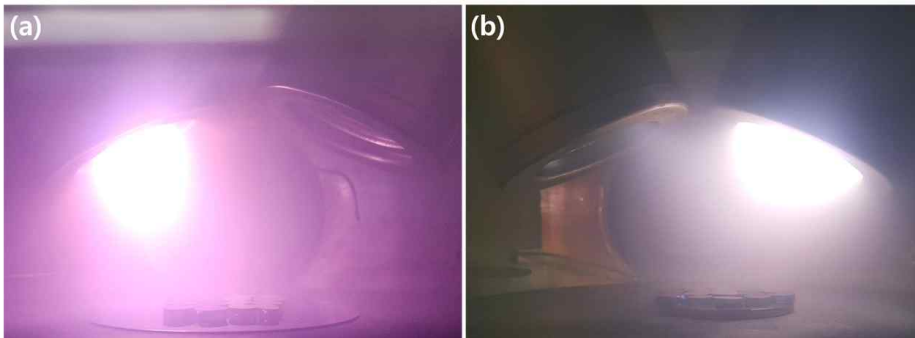
Fig. 11. Plasma images of magnetron sputtering treatment using Zr-HA target: (a) Zr target sputtering image, and (b) HA target sputtering image.

Ⅲ. 5. Analysis of surface properties of Ti-40Nb-xTa alloys

Utilizing a field emission scanning electron microscope (FE-SEM; Hitachi 4800, Japan) and an energy dispersive X-ray spectrometer, the surface characteristics of the surface-treated Ti-40Nb-xTa alloy were examined (EDS; Hitachi 4800, Japan). For shape and composition analysis, the operating voltage was set to 15 kV, the scan speed of FE-SEM was set to 40 seconds, and the activation time of EDS was set to 30 seconds. The pore size, shape, and porosity of the surface-treated Ti-40Nb-xTa alloy were measured using an image analyzer (Image J, Wayne Pasband, USA) program.

Through the use of X-ray diffraction (XRD, X'pert Philips, Netherlands), the surface's crystal structure was examined. The diffraction angle range of 20° ~ 90° was used with Cu Kα radiation (λ = 1.5418). The analysis was performed. The crystal structure according to the XRD peak was confirmed by comparison with the Joint Committee on Power Diffraction Standards (JCPDS, PCPDFWIN). The cross-section of the Ti-40Nb-xTa alloy was observed by FE-SEM, EDS line profiling, and Backscattered Electron (BSE; Hitachi 4800, Japan) to analyze the thickness of the oxide film after the PEO process. And a quantitative estimate of oxide film thickness was calculated using ImageJ software. When the backscattered electrons hit the detector, they create the signal used to form the TV image. All elements have nuclei of different sizes, and the number of BSEs increases as the size of the atomic nucleus increases. Therefore, BSE can be used to obtain images showing the various elements present in the sample.

Ⅲ. 6. Mechanical properties test

Ⅲ. 6. 1. Surface roughness measurement

An atomic force microscope (AFM; Park XE-100, Park Systems, Korea) was used to measure the alloy's surface roughness. and analyzed using the XE Data Acquisition program. Non-contact AFM analysis was measured at a scan rate of 0.50 Hz and a scan size of 15.00 μm.

Ⅲ. 6. 2. Measurement of hardness and elastic modulus using nano-indentation

The elastic modulus and hardness of the alloy surface were measured using a nanoindentation tester (TTX-NHT3, Anton Paar, Austria). The load application and removal times were each set to 30 seconds, the maximum load was 20 mN, and the stop time was 5 seconds. To determine the average value and standard deviation of each sample, measurements were performed five times.

Ⅲ. 6. 3. Coating adhesion using scratch test

To ascertain the coated surface's adherence, a scratch test (ST30, J&L Tech, Korea) was carried out. The load was applied gradually from an initial load of 0.5 N to a final load of 20 N. A scratch experiment was conducted at a speed of 0.22 mm/s for a length of 5 mm using a diamond indenter with r = 200 μm. In addition, LC1 stands for the area where the initial scratch appeared, and LC2 for the area where the base material becomes visible as the coating layer is peeled away.

Ⅲ. 7. Measurement of surface wettability

A contact angle goniometer was used to test the surface's wettability (KSA100, Kruss, Germany). Using a video camera and a contact angle meter, automatically falling water droplets were used to determine the contact angle using the static droplet method. For the experiment, 6 μl of distilled water was dropped in the form of drops using a needle at room temperature, and the average value and standard deviation were obtained by measuring 5 times for each sample. The contact angle measurement mechanism is shown in Fig. 12 [47].
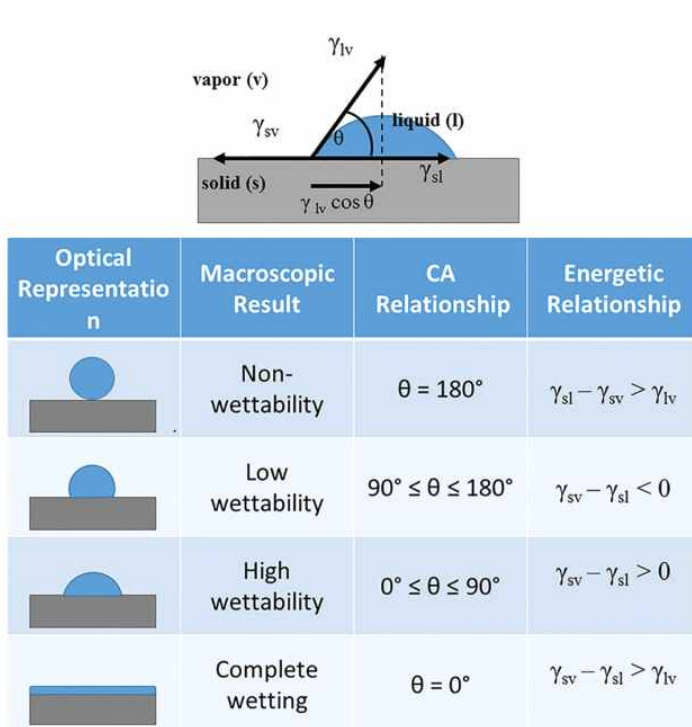
Fig. 12. Mechanism of wettability measurement on the substrate [47].

Ⅲ. 8. Electrochemical corrosion test

The electrochemical properties of the Ti-40Nb-xTa alloy were investigated using electrochemical measurements using a three-electrode electrochemical setup. A high-density carbon rod served as the counter electrode, a saturated calomel electrode served as the reference electrode, and a sample was connected to the working electrode. As the test solution, a 0.9% NaCl solution was used while maintaining the temperature at 36℃ ± 1 like body temperature. Potentiodynamic polarization tests for corrosion behavior were performed using a potentiostat (PARSTAT MC, AMETEK, USA) from -1500 to 1500 mV with a scan rate of 1.67 mV/s. Corrosion potential (E_{corr}) and corrosion current density (I_{corr}) were then measured using the Tafel line analysis of polarization curves.

Ⅲ. 9. Hydroxyapatite crystallization in simulated body fluid (SBF) solution

To investigate the biological activity (hydroxyapatite-forming ability) of the sample, the sample was immersed in a biosimilar solution (SBF, Simulated Body Fluid) for 24 hours. The SBF solution was maintained at 36.5 ± 1℃, the same as the human body temperature, and the detailed ion concentration of the SBF solution is shown in Table 5. The pH concentration was maintained at 7.4 ± 0.5 using tris(hydroxymethyl) aminomethane, 99.0% ($C_4H_{11}NO_3$ = 121.14) and 1:9 HCl (hydrochloric acid, 36.46 g/mol). After the test, the item was rinsed with distilled water, dried naturally, and placed in a beaker with 1000 ml of SBF solution.

Table 5. Concentration of SBF solution and human plasma

Ions	Concentration (mM)	
	Blood plasma	**SBF**
Na^+	142.0	142.0
K^+	5.0	5.0
Mg^{2+}	1.5	1.5
Ca^{2+}	2.5	2.5
Cl^-	103.0	103.0
HCO_3^-	27.0	10.0
HPO_4^-	1.0	1.0
SO_4^{2-}	0.5	0.5

Ⅳ. RESULTS AND DISCUSSION

Ⅳ. 1. Microstructure and phase analysis of Ti-40Nb-xTa alloys

Figure 13 shows the results of XRF spectrum for Ti-40Nb, Ti-40Nb-3Ta, Ti-40Nb-7Ta, and Ti-40Nb-15Ta alloys, respectively. Figure 13 shows (a) Ti-40Nb, (b) Ti-40Nb-3Ta, (c) Ti-40Nb-7Ta, and (d) Ti-40Nb-15Ta alloys, respectively. Figure 13 (a) shows that no Ta peak was detected because Ta was not added. In Figure 13 (b ~ d), it was observed that the peaks of Ta increases as the content of Ta increases. As a result of XRF analysis of the alloy homogenized through heat treatment after manufacturing, it can be confirmed that the chemical composition is similar to the designed alloys, and the chemical composition of the analyzed alloy is shown in Table 6.

Figure 14 shows the microstructure images of Ti-40Nb-xTa according to the Ta content observed with an optical microscope. Figure 14 (a) is a microstructure of images for Ti-40Nb, (b) Ti-40Nb-3Ta, (c) Ti-40Nb-7Ta, and (d) Ti-40Nb-15Ta alloys. Figure 14 (a) shows two microstructures of martensitic needle structure (α") and equiaxed structure (β) were observed. Also, it can be observed that the martensitic structure decreases as the Ta content increases as shown in Figure 14 (b ~ d). This is because Nb and Ta are β-stabilizing elements of Ti, and when the β-stabilizing element is alloyed with Ti, it lowers the phase transformation point, which changes from β to α. For this reason, when homogenizing through rapid cooling under the same conditions after heat treatment, the β phase, which is a high-temperature stable phase, can easily remain as a metastable phase at room temperature [24, 48]. In addition, it can reduce or prevent the formation of martensitic structure by suppressing the formation of α phase, which is a low-temperature stable phase [49].

Figure 15 shows the XRD patterns of Bulk Ti–40Nb–xTa alloys. Figure 15 (a ~ d)

shows 0Ta, 3Ta, 7Ta, and 15Ta, respectively. The α"-phase (orthorhombic) and β body-centered cubic (BCC) phases showed in the Ti-40Nb-xTa alloy. Equiaxed β-phase peaks were appeared at 2Θ = 38.57°, 55.74°, and 70.18°, while martensite α" phase peaks were appeared at 2Θ = 52.69°, 68.16°, 73.88°, and 84.21°. The α" phase peaks at 2Θ = 52.69°, 73.88° and 84.21° detected in Ti-40Nb were not detected in the Ta-added alloy. And 2Θ = 68.16° is detected only in Ti-40Nb alloy and Ti-40Nb-3Ta alloy because the α" phase peak decreases with increasing Ta content. For Ti-40Nb and Ti-40Nb-3Ta, α" and β-phase peaks were observed, and only β-phase peaks were observed for Ti-40Nb-7Ta and Ti-40Nb-15Ta. This shows that the alloy changes from α"+β phase to β phase by increasing Ta contents. This XRD result is also consistent with Figure 14, where the microstructure was observed under an optical microscope. As the Ta content of the Ti-40Nb-xTa alloys increased, the FWHM (full width at half maximum) of x-ray peaks became narrower, which means that the alloys were crystallized and transformed to beta phase and the hardness decreased [50]. However, the alloy's grain size decreases when Ta content is raised to 15%, which is expected to slightly increase hardness.
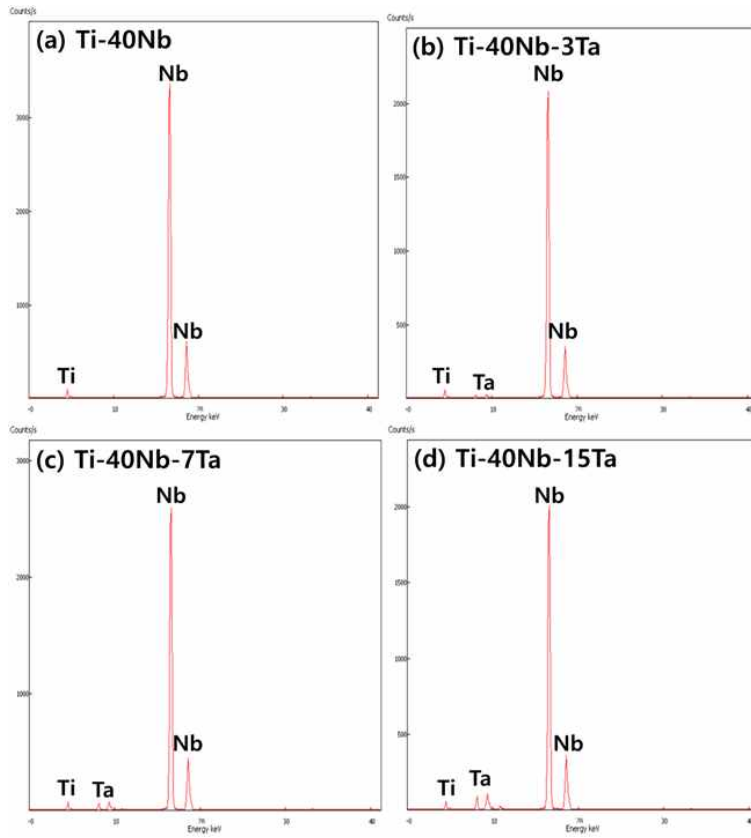
Fig. 13. XRF analysis of Bulk Ti-40Nb-xTa alloys: (a) 0Ta, (b) 3Ta, (c) 7Ta, and (d) 15Ta.

Table 6. XRF analysis of Bulk Ti-40Nb-xTa alloys

Specimen \ Element (%)	Ti	Nb	Ta
0Ta	59.82 ± 0.33	40.18 ± 0.33	0
3Ta	57.45 ± 0.38	39.25 ± 0.41	3.30± 0.05
7Ta	53.14 ± 2.05	39.89 ± 1.50	6.98 ± 0.62
15Ta	45.11 ± 1.37	39.11 ± 0.72	15.77 ± 0.89
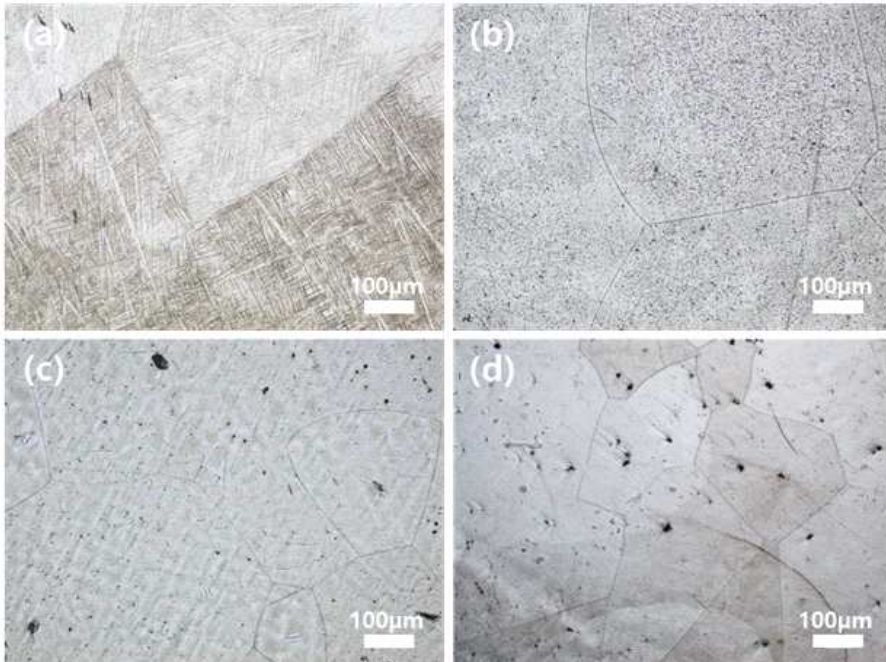
Fig. 14. Optical micrographs of Bulk Ti-40Nb-xTa alloys: (a) 0Ta, (b) 3Ta, (c) 7Ta, and (d) 15Ta.
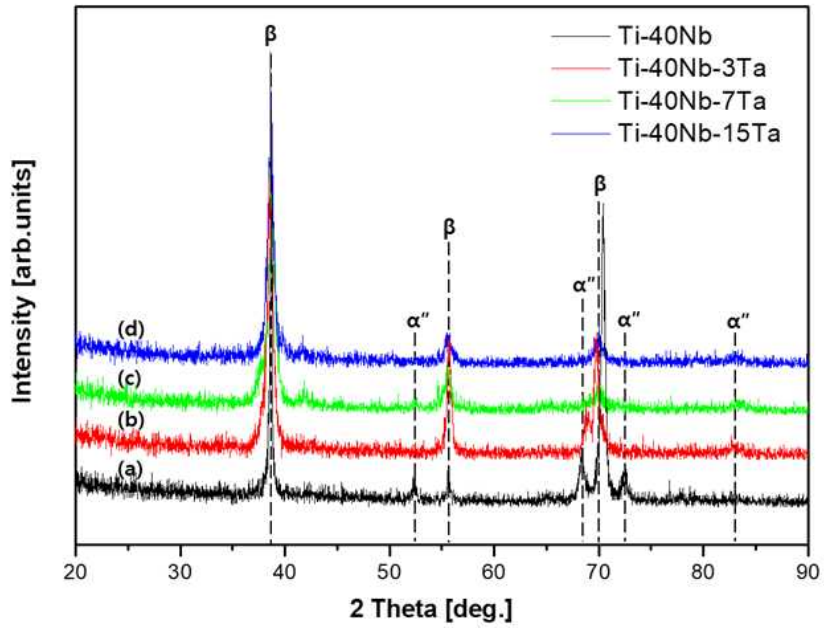
Fig. 15. XRD results of Bulk Ti-40Nb-xTa alloys: (a) 0Ta, (b) 3Ta, (c) 7Ta, and (d) 15Ta.

IV. 2. Hardness and Elastic modulus test of Ti-40Nb-xTa alloys

The results of a nano-indentation test on a Ti-40Nb-xTa alloy that had been heated to 1050℃ for 1 hour in an environment of argon gas are shown in Figure 16. The hardness and elastic modulus of the alloy could be measured by the nano-indentation test, and the results were shown in the bar graph and load-displacement graph in Figure 16, and the measured values are shown in Table 7. As a result of nano-indentation measurement, the elastic modulus of the Ti-40Nb alloy was 94.82 GPa, and the elastic modulus of the Ti-40Nb-xTa alloy gradually decreased as the Ta content increased. This is because the addition of β-stabilizing elements such as Nb and Ta to titanium increases the inner lattice distance and reduces the elastic modulus [51]. Ti-40Nb-7Ta was the lowest at 62.94 GPa, and it was reduced by about 57% compared to the elastic modulus of 110 GPa of Ti-6Al-4V alloy, which is most commonly used as an implant material. According to expectations, the Ti-40Nb-xTa alloy will have a lower modulus of elasticity than human bone, reducing the stress-shielding effect between the implant and bone [21]. As a result of the load-displacement graph, based on Ti-40Nb, which has the highest hardness, as the addition of Ta contents to Ti-40Nb alloy, hardness decreased and the elastic modulus decreased. When the Ta content increases to 15%, the hardness increases again, which is thought to be related to the increase in grain size as discussed above.
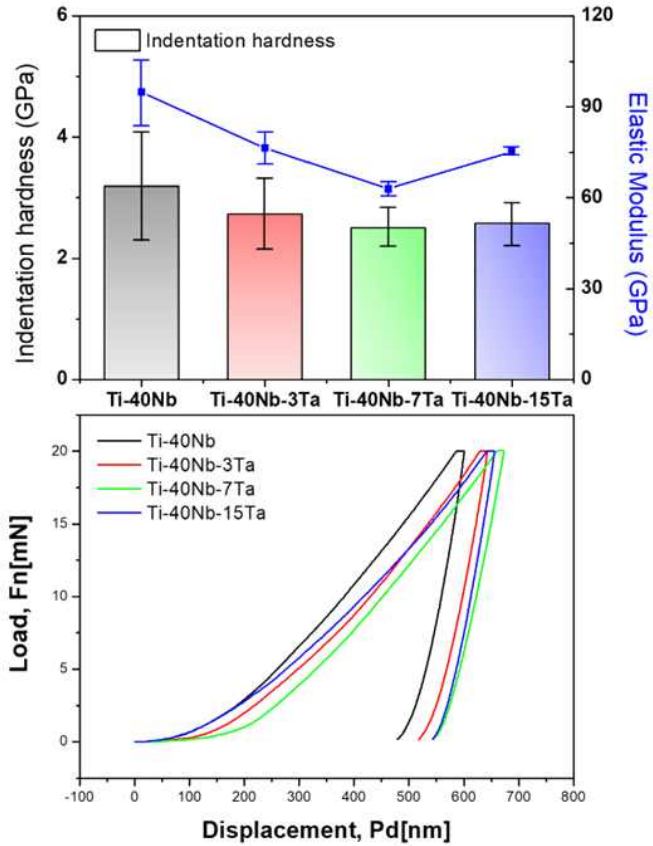
Fig. 16. Results of bulk Ti-40Nb-xTa alloys' nano-indentation tests: (a) 0Ta, (b) 3Ta, (c) 7Ta, and (d) 15Ta.

Table 7. Ti-40Nb-xTa alloys' elastic modulus and nano-indentation hardness

Specimen	Ti-40Nb-xTa			
	0Ta	3Ta	7Ta	15Ta
Indentation hardness (GPa)	3.19 ± 0.94	2.73 ± 0.59	2.51 ± 0.36	2.58 ± 0.40
Elastic modulus (GPa)	94.82 ± 20.63	75.45 ± 11.84	62.94 ± 4.11	75.21 ± 2.95

Ⅳ. 3. Surface properties of Ti-40Nb-xTa alloy after plasma electrolytic oxidation (PEO)

Figure 17 shows spark discharges appearing on the Ti-40Nb-xTa alloy surface during the PEO process in an electrolyte containing calcium and phosphorus ions. Figure 17 (a ~ d) shows spark discharge images of 0Ta, 3Ta, 7Ta, and 15Ta, respectively. An oxide film is created in 0.04 seconds after the start of PEO treatment, and bubbles and spark discharge occur vigorously. Regardless of the alloy's Ta ratio, all coatings were the same, and irregular spark discharges were actively displayed over the entire surface for up to 5 seconds. The irregular sparks on the metal surface then grew longer as the Ta concentration was increased. It is expected that this spark discharge will have an effect on the pore shape of the alloy surface. Spark discharge was formed steadily before 10 seconds, but was rarely formed from 10 seconds to 180 seconds. In general, the PEO process occurs when a high voltage is applied after configuring a circuit in an electrolyte. When a voltage is applied to the configured circuit, the surface of the alloy is oxidized to form an oxide film serving as a thin insulating layer, and insulation breakdown and sparks occur. The generated spark melts the metal surface, and the molten metal surface rapidly solidifies upon contact with the electrolyte. The ions in the electrolyte are contained in the oxide film during this coagulation reaction, and the thickness and structure of the oxide film change as a result of the further created micro discharge [52, 53].

Figure 18 depicts the findings of FE-SEM analysis of the pore structure developed on the Ti-40Nb-xTa alloy surface following PEO treatment. According to the Ta concentration, different types of irregular pores formed on the alloy surface, as shown in Figure 18. Long worm-shaped pores were found from Ti-40Nb-7Ta, and long worm-shaped pores were produced over the whole surface of the Ti-40Nb-15Ta alloy as the Ta component of the alloy increased. It is thought that spark discharge occurred for a long period on the surface as the Ta content of the Ti-40Nb-xTa alloy increased during the PEO treatment. During the PEO process, it occurs where the sparking surface has the weakest resistance. Due to the initial spark, the pores of the crater

model are formed, and when additional sparks occur, sparks are generated at the place with the weakest resistance. The size of the pore increases and connects to form a worm-shaped pore [54]. Ca and P elements were distributed arround the pores on the alloy surface by FE-SEM observation at high magnification.

Figure 19 displays the outcome of using the Image J program to analyze the pores formed on the alloy surface by the PEO treatment (Wayne Rasband, USA). Measurements were made of the porosity, number, and fraction of pores. Figure 19 and Table 8 display the analysis's results, and they reveal that as the Ta content increase, the pore size increase. As a result, the porosity tends to increase while the number of pores per unit area (2500 μm^2) tends to decrease. Additionally, the fraction of pores increased as the Ta content increased. This suggests that the size, quantity, and porosity can be adjusted in accordance with the Ta concentration.

The Ti-40Nb-xTa alloy's EDS data for the PEO process in an electrolyte containing Ca and P ions are shown in Figure 20. The EDS results of Ti-40Nb, Ti-40Nb-3Ta, Ti-40Nb-7Ta, and Ti-40Nb-15Ta are shown in Figures (a ~ d), respectively. It was not detected in Figure 20(a) because the Ta element was not added, and in Figures (b ~ d), the Ta element peak increased as the Ta content increased. In addition, Ca and P ions in the electrolyte during the PEO treatment were detected throughout the Ti-40Nb-xTa alloy. Hydroxyapatite (HA) has a stoichiometric Ca/P ratio of 1.67 wt.%, which is chemically and structurally similar to living bones, helping to form and grow human bone nuclear [55]. Therefore, it should be similar to 1.67 wt.% to promote high bioactivity between bone and dental implant, and the EDS results for Ti-40Nb-xTa alloy were similar, 1.61, 1.63, 1.60, and 1.68 wt.%, respectively.

Figure 21 is a cross-section of the Ti-40Nb-xTa alloy observed by FE-SEM, EDS line profiling, and Backscattered Electron (BSE) to analyze the thickness of the oxide film after the PEO process. Through the FE-SEM image in Figure 21, pores inside of the oxide layer could be observed, and the boundary between the coating layer and the alloy could be clearly distinguished by BSE analysis, when there are many elements present, the surface appears white. The alloying elements of Ta, Nb, and Ti, which are relatively heavier than Ca, P, and O, which are components of the oxide film, were observed as bright images. As a result, line profiling can be used to check the coating

layer's thickness, oxygen can be distributed in the coating layer due to the TiO_2 layer created by the PEO treatment, and Ca and P from the electrolyte were also found there. In contrast, the alloy contained the alloying elements of Ti, Nb, and Ta.

Figure 22 and Table 9 show the thickness of the oxide film observed in Figure 21 after analysis using the Image J program. Due to this, the oxide film's thickness increased as the Ta content increased, just like the pore size increased. Figure 17's spark discharge duration appears to be relevant here, as the Ti-40Nb-15Ta alloy with the longest discharge time exhibited the thickest oxide deposit.

Ti-40Nb-xTa's XRD pattern after PEO treatment in an electrolyte containing Ca and P ions is depicted in Figure 23. 0Ta, 3Ta, 7Ta, and 15Ta are shown in Figure 23 (a ~ d). Anatase, rutile, Nb_2O_5, Ta_2O_5, and HA crystal phases were observed, and anatase and rutile are one of the representative crystal phases of TiO_2 oxide. Due to the crystallographic link between the (110) plane of anatase and the (0001) plane of biomimetic apatite, the most ideal form, anatase is known to be more advantageous for the manufacture of apatite than other Ti oxide phases [56]. However, in the crystal structure of TiO_2 of titanium, when Nb and Ta elements are added, the formation of Nb_2O_5 and Ta_2O_5 increases, preventing the formation of TiO_2 phase and HA crystal phase, so the peak decreases [57].
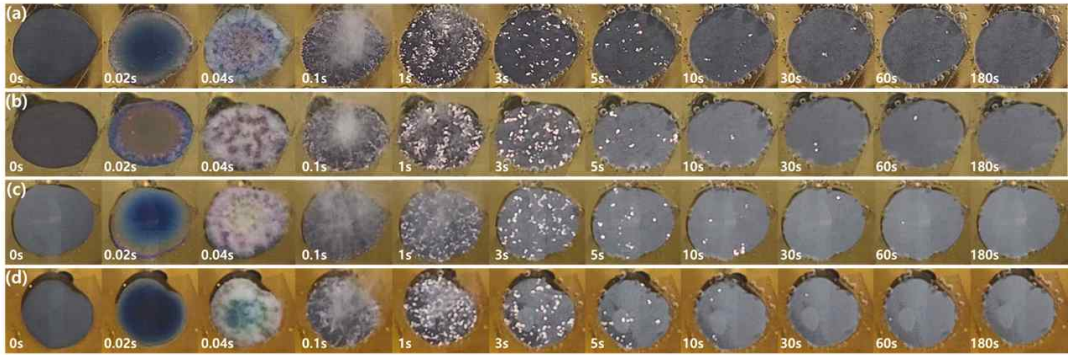
Fig. 17. Evolution of spark discharge during the PEO of Ti-40Nb-xTa alloys: (a) 0Ta, (b) 3Ta, (c) 7Ta, and (d) 15Ta.
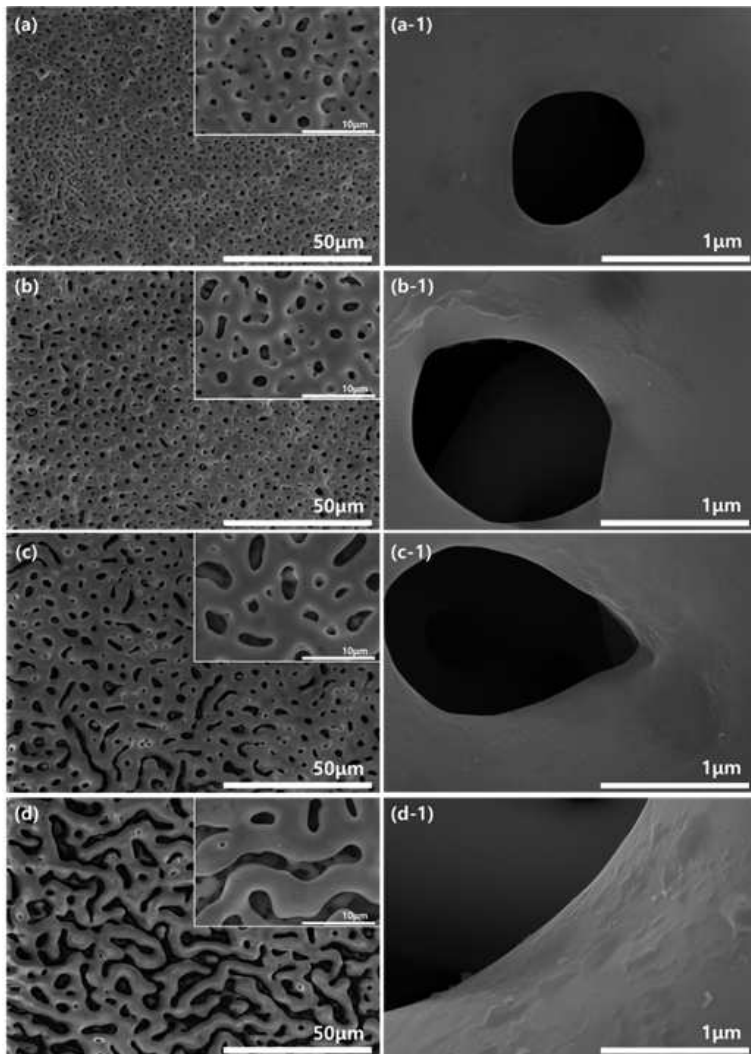
Fig. 18. FE-SEM images of PEO surface treatment on Ti-40Nb-xTa alloys: (a) 0Ta, (a-1) high magnification of 0Ta, (b) 3Ta, (b-1) high magnification of 3Ta, (c) 7Ta, (c-1) high magnification of 7Ta, (d) 15Ta, and (d-1) high magnification of 15Ta.
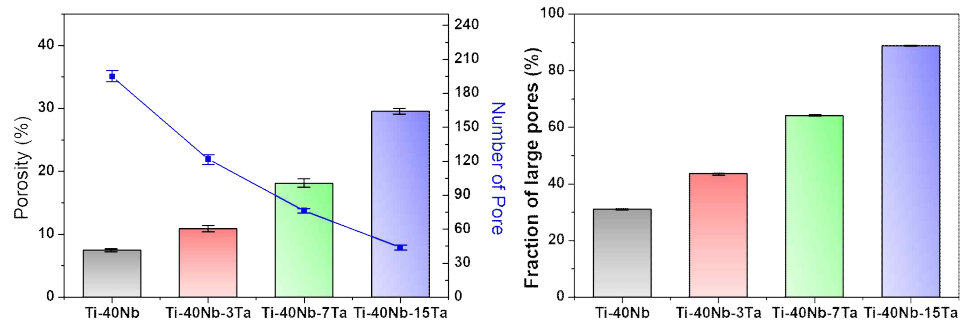
Fig. 19. Pore formation results on Ti-40Nb-xTa alloys after PEO treatment : (a) porosity and number of the pore, (b) fraction of large pores.

Table 8. Pore analysis of PEO-treated surface on Ti-40Nb-xTa alloys

Specimens	Ti-40Nb-xTa			
	0Ta	3Ta	7Ta	15Ta
Porosity (%)	7.47 ± 1.13	10.92 ± 1.67	18.11 ± 2.57	38.67 ± 1.41
Number of pore (2500 μm^2)	194.82 ± 6.29	121.77 ± 7.10	76.24 ± 5.74	43.83 ± 5.80
Fraction of large pore (100 μm^2)	31.11 ± 0.41	43.71 ± 0.81	64.23 ± 0.56	88.90 ± 0.34
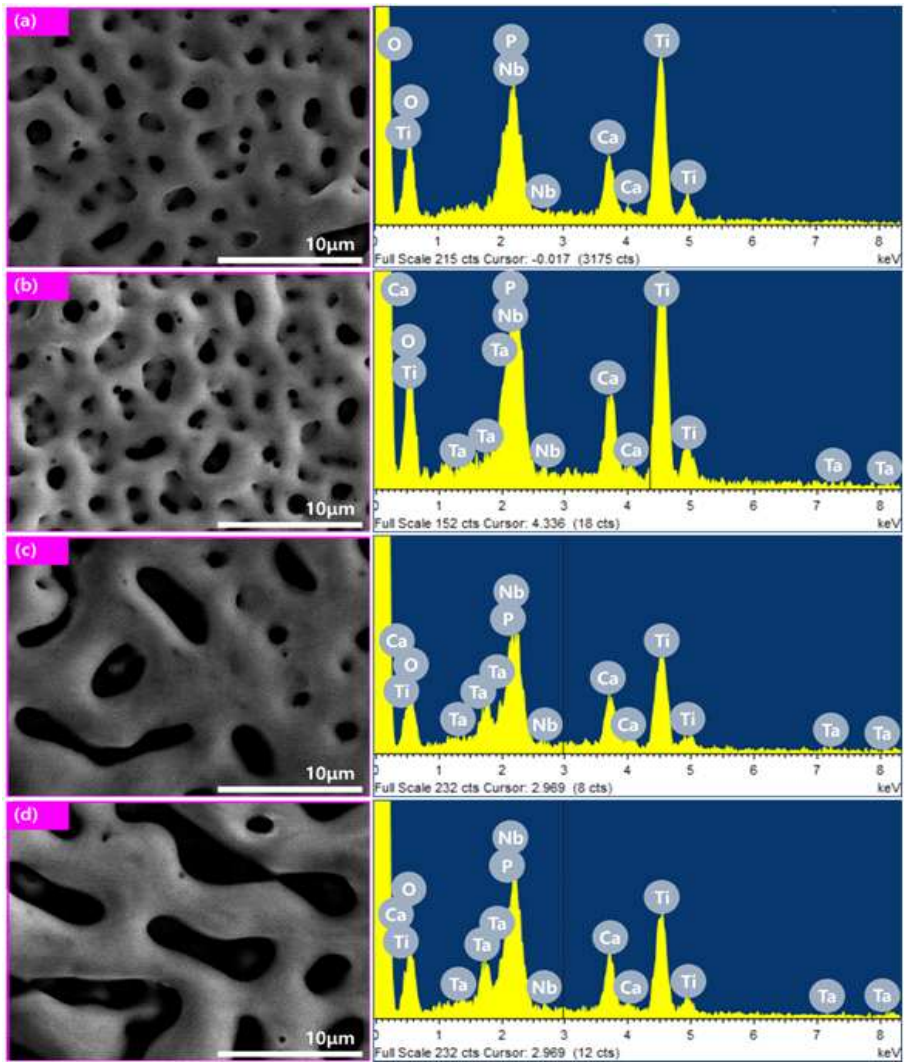
Fig. 20. EDS results of PEO treatment on Ti-40Nb-xTa alloys: (a) 0Ta, (b) 3Ta, (c) 7Ta, and (d) 15Ta.
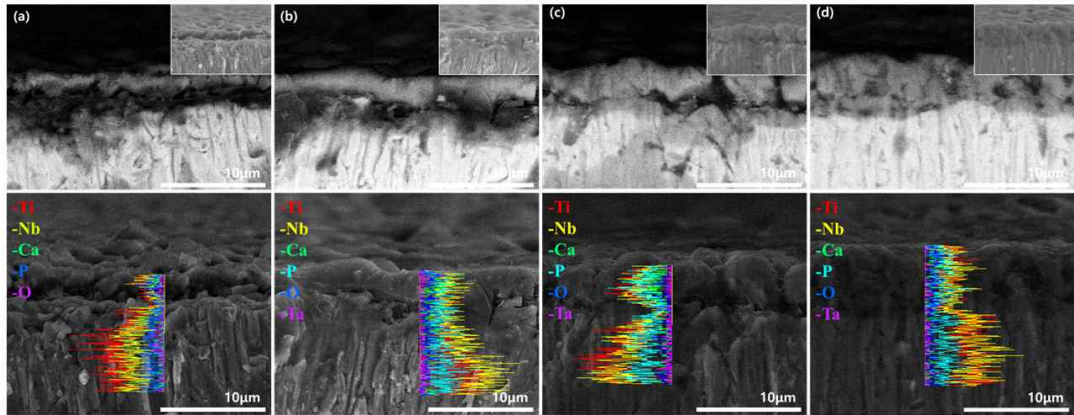
Fig. 21. FE-SEM images and EDS line profiling of the oxide layer formed by PEO treatment on Ti-40Nb-xTa alloys: (a) 0Ta, (b) 3Ta, (c) 7Ta, and (d) 15Ta.
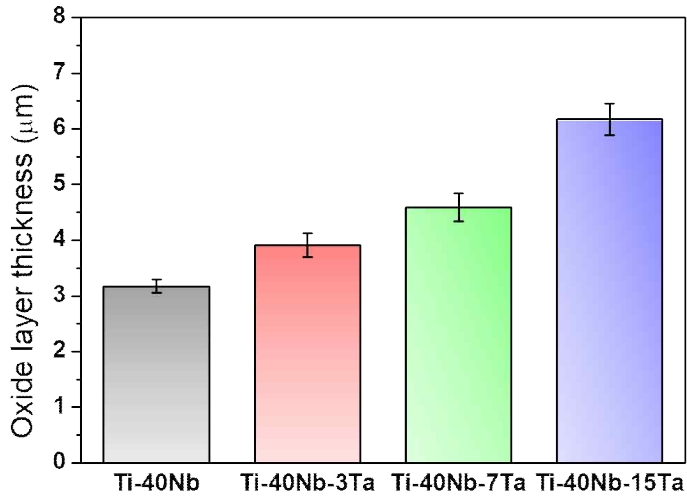
Fig. 22. Oxide layer thickness formed by PEO treatment on Ti-40Nb-xTa alloys.

Table 9. Oxide layer thickness measurements value of alloys of Ti-40Nb-xTa with PEO surface treatment

Samples	Ti-40Nb-xTa			
	0Ta	3Ta	7Ta	15Ta
Thickness of oxide layer (μm)	3.17 ± 0.12	3.91 ± 0.21	4.59 ± 0.25	6.17 ± 0.28
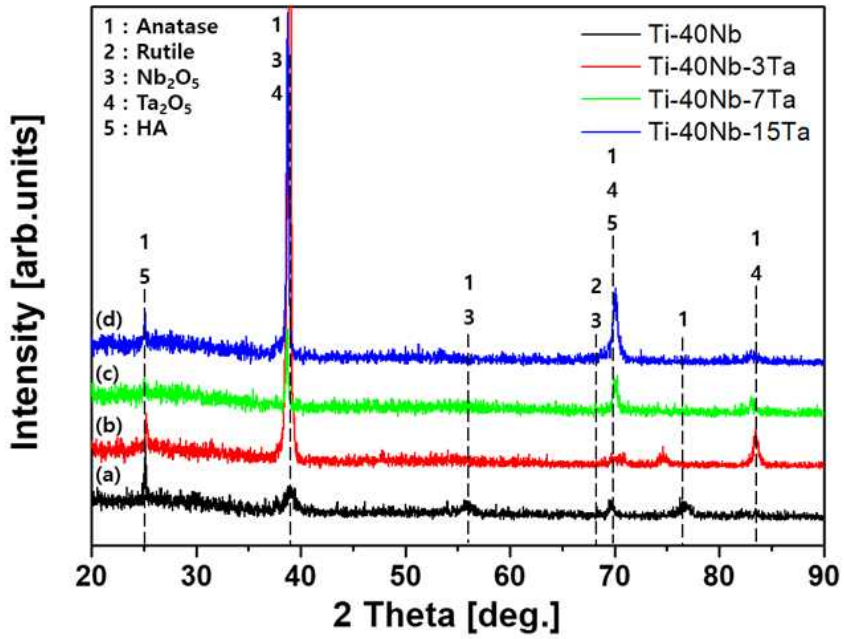
Fig. 23. XRD results of alloys of Ti-40Nb-xTa with PEO treatment; (a) 0Ta, (b) 3Ta, (c) 7Ta, and (d) 15Ta.

Ⅳ. 4. Surface properties of Ti-40Nb-xTa alloys coated with hydroxyapatite (HA) and zirconium (Zr) by RF-magnetron sputtering

Figure 24 shows images observed by FE-SEM after PEO treatment followed by a Zr-HA coating on the alloy surface using RF-magnetron sputtering. In Figure 24, surface morphology with treated by HA-Zr shows the similar SEM images compared to that of PEO treatment. However, presence of Zr-HA was confirmed through high magnification SEM observation. On the surface of the oxide film, the Zr-HA particles can be seen to be uniformly covered in a circular pattern. This indicates that the Zr-HA coating layer was thinly coated.

The EDS analysis results are shown in Figure 25 and compared to the results after PEO surface treatment in Figure 20, more Ca and P elements were detected and Zr elements were observed after Zr-HA coating. The effectiveness of the Zr-HA coating was confirmed by FE-SEM pictures and EDS analytical findings.

Figure 26 shows the findings of the XRD analysis of the PEO + Zr-HA alloy. Figure 26 (a ~ d) are 0Ta, 3Ta, 7Ta and 15Ta, respectively. Many peaks similar to the xrd analysis pattern in Figure 23 were observed, and the $2\Theta = 32.77°$ and $43.15°$ peaks, which appear to be caused by HA, were additionally analyzed, and the $2\Theta = 56.92°$ peak appeared stronger than the XRD analysis pattern in Figure 23. Also, the Zr peaks $2\Theta = 69.52°$, $73.02°$ were analyzed. The Zr-HA coating film was thin peaks similar to those of the PEO treatment on alloy were observed.

Figure 27 shows the scratch test results of Zr-HA coated surface on PEO treatment on Ti-40Nb-xTa alloys. Figure 27 (a ~ d) is 0Ta, 3Ta, 7Ta, and 15Ta, respectively. When comparing the Lc1 values at which scratches began for each alloy, the load was gradually applied, and it tended to increase as the Ta content increase. The strength of the surface adhesion increases along with the Ta content. In addition, comparing the Lc2 value based on the point where the coating is peeled off and the base material is exposed, it can be seen that the film adhesive strength also increases as the Ta content increases. The reason for this can be found through the cross section observation. That is, in Figures 21 and 22 and Table 9 after PEO treatment, the oxide film coating layer

becomes thicker according to the Ta content and it is thought that this is because coatings of various other oxides were formed.

Figure 28 is the anodic polarization curve obtained for the Zr-HA coated surface sample by RF-magnetron sputtering on the PEO surface treatment on Ti-40Nb-xTa alloy. Corrosion potential (E_{corr}) from the polarization curve indicated the highest at ‑334 mV of Ti-40Nb-15Ta and the lowest at ‑790 mV of Ti-40Nb in the case of bulk. From this result, it was confirmed that corrosion potential value and corrosion resistance were increased according to the content of Ta, which was the same in the Zr-HA coated alloy. Additionally, Zr and HA had a beneficial impact on enhancing corrosion resistance in the case of Zr-HA coating since overall corrosion potential increased and current density reduced in comparison to bulk. Each value is listed in Table 9. However, a stable oxide film was formed as a result of the formation of an oxide film during the PEO treatment. When Zr and HA are coated, corrosion resistance is greatly increased due to the formation of an oxide film from Zr coated on the surface during the corrosion process, and corrosion by pores is prevented to some extent by being coated on the part where pores are formed [58].
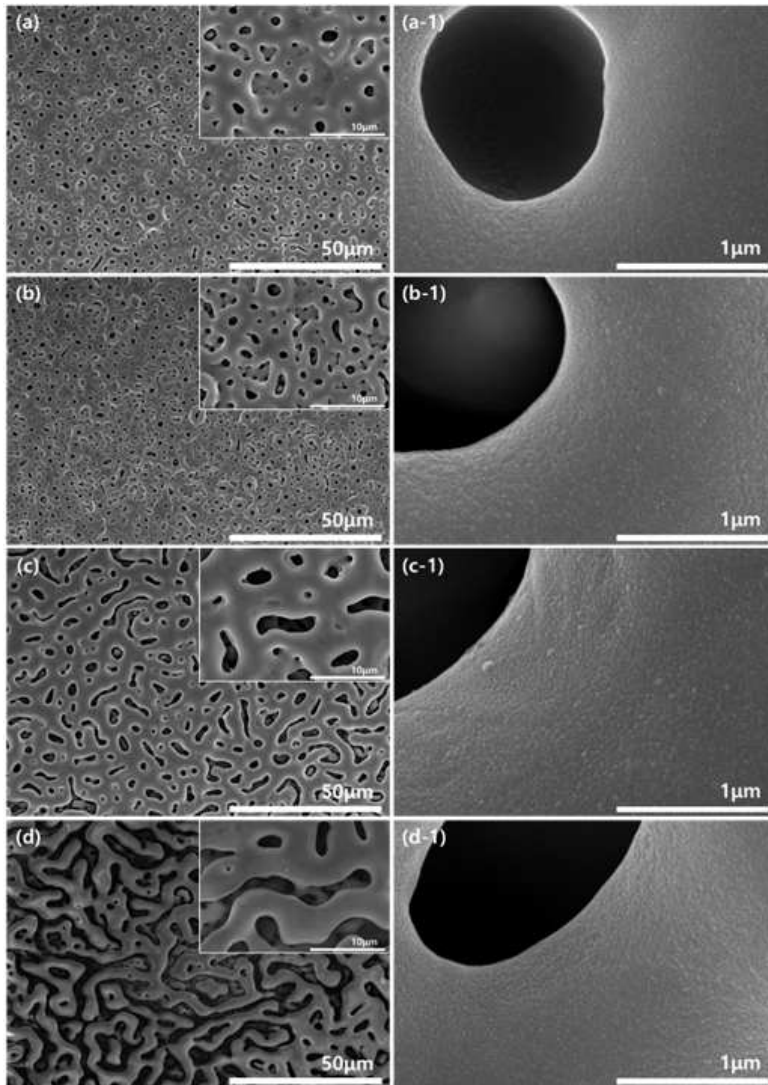
Fig. 24. FE-SEM images of PEO treatment on Ti-40Nb-xTa alloys with RF-magnetron sputtered Zr-HA coatings: (a) 0Ta, (a-1) high magnification of 0Ta, (b) 3Ta, (b-1) high magnification of 3Ta, (c) 7Ta, (c-1) high magnification of 7Ta, (d) 15Ta, and (d-1) high magnification of 15Ta.
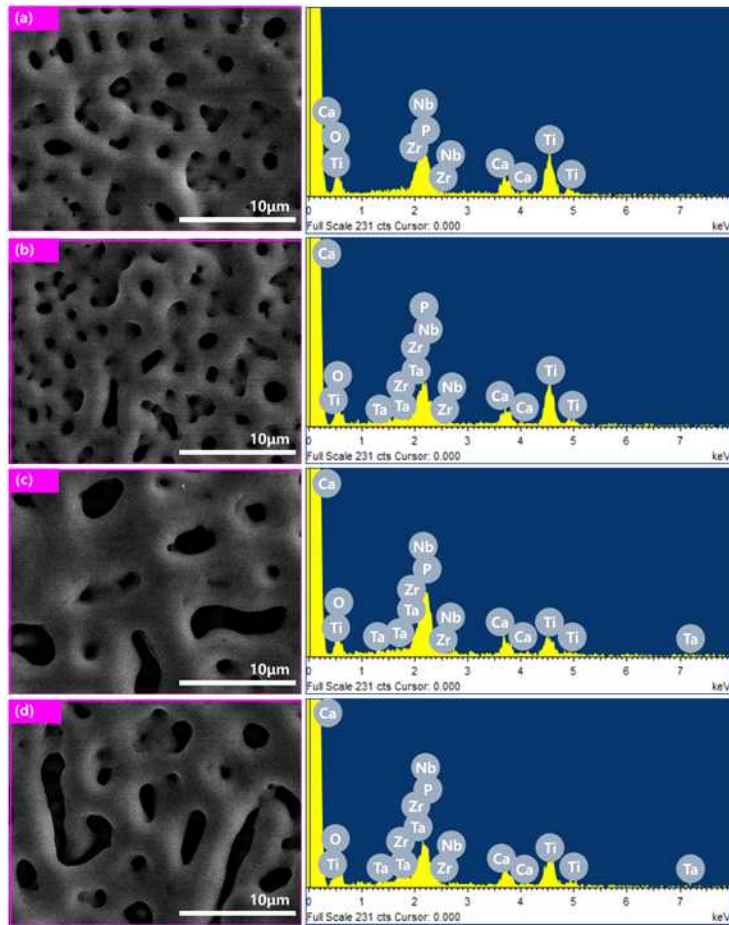
Fig. 25. EDS results of Zr-HA coated surface by magnetron sputtering on PEO treatment on Ti-40Nb-xTa alloys: (a) 0Ta, (b) 3Ta, (c) 7Ta, and (d) 15Ta.
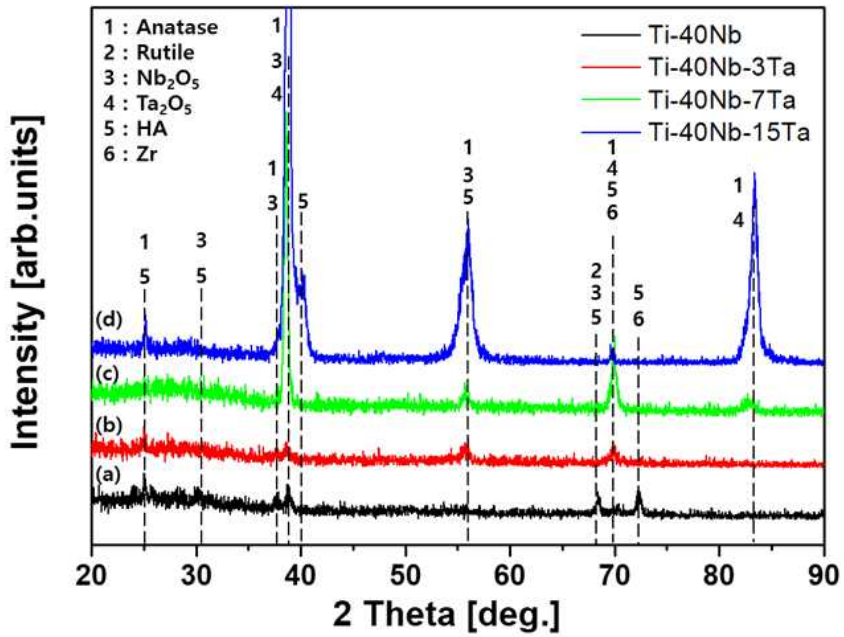
Fig. 26. XRD results of Zr-HA coated surface by RF-magnetron sputtering on PEO-treated Ti-40Nb-xTa alloys: (a) 0Ta, (b) 3Ta, (c) 7Ta, and (d) 15Ta.
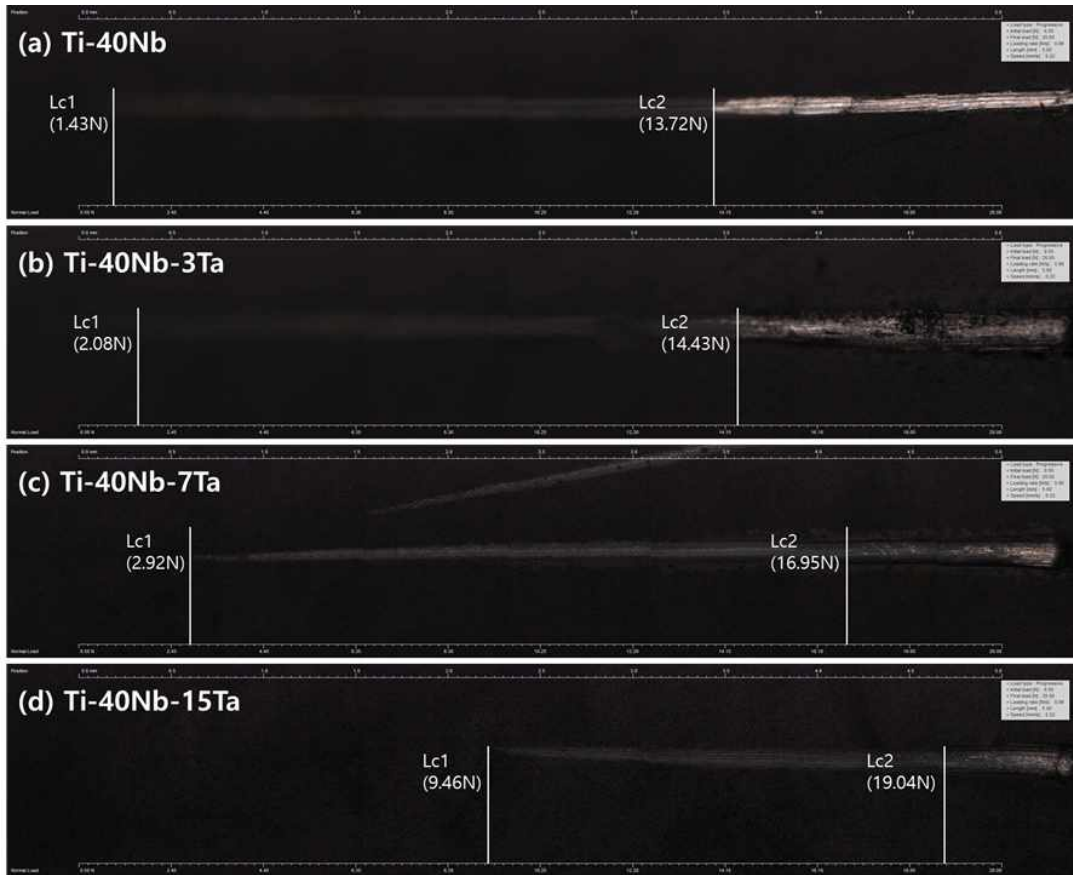
Fig. 27. The scratch test results of Zr-HA coated surface by RF-magnetron sputtering on PEO-treated Ti-40Nb-xTa alloys: (a) 0Ta, (b) 3Ta, (c) 7Ta, and (d) 15Ta.
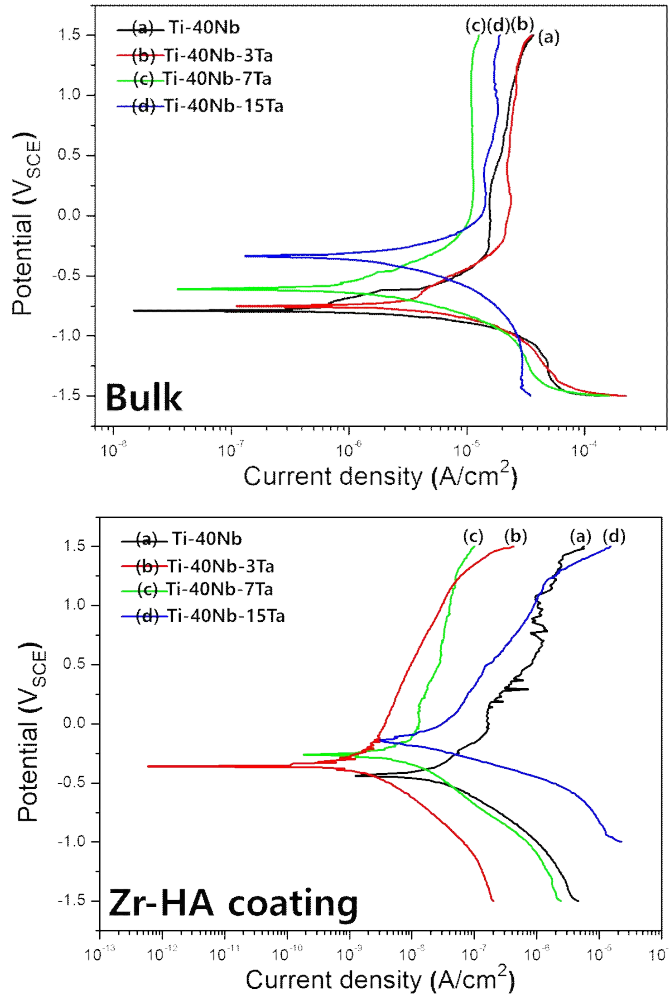
Fig. 28. Potentiodynamic polarization curves of bulk Ti-40Nb-xTa alloys and Zr-HA coated surface by RF-magnetron sputtering on PEO-treated Ti-40Nb-xTa alloys: (a) 0Ta, (b) 3Ta, (c) 7Ta, and (d) 15Ta.

Table 10. Results of potentiodynamic polarization using Tafel plots

Specimens	Bulk				Zr-HA coating			
	0Ta	3Ta	7Ta	15Ta	0Ta	3Ta	7Ta	15Ta
E_{corr} (mV)	-790	-751	-599	-334	-439	-374	-249	-135
I_{350mV} (A/cm^2)	1.70×10^{-5}	2.21×10^{-5}	1.13×10^{-5}	1.39×10^{-5}	4.02×10^{-7}	1.89×10^{-8}	6.50×10^{-9}	1.10×10^{-7}
I_{corr} (A/cm^2)	1.49×10^{-8}	1.14×10^{-7}	3.49×10^{-8}	1.31×10^{-7}	1.25×10^{-9}	6.57×10^{-13}	1.99×10^{-10}	2.74×10^{-9}

Ⅳ. 5. Biocompatibility of surface-treated Ti-40Nb-xTa alloys

Ⅳ. 5. 1. Surface roughness of Ti-40Nb-xTa alloys according to surface treatment method

Figure 29 shows the surface topologies of etched bulk, PEO and PEO + sputtering using AFM. Table 10 shows the mean roughness values obtained through AFM analysis. In the case of bulk alloy, the roughness value changes due to the change of microstructure, and it changes from α"+β phase to β phase as shown in Figure 14. That is, as the equiaxed structure of the α"+β phase shifted to the β phase, the roughness steadily diminished. In the case of PEO, tiny holes developed, and overall roughness greatly increased when compared to bulk. The diameter also increases with the Ta content. And as oxide layer thickness and the Ta content increase, the roughness tends to get rougher. The case of PEO + sputtering is similar to the roughness of PEO, which is considered to have little effect on the roughness value because the coated Zr-HA thin film is very thin. Cells adhered implants have different growth and differentiation depending on the surface roughness, so it acts on an important key factor for biocompatibility [59]. It is also known that the roughness range of 50 nm to 1.2 μm has a significant effect on the initial adhesion of bone cells [60].
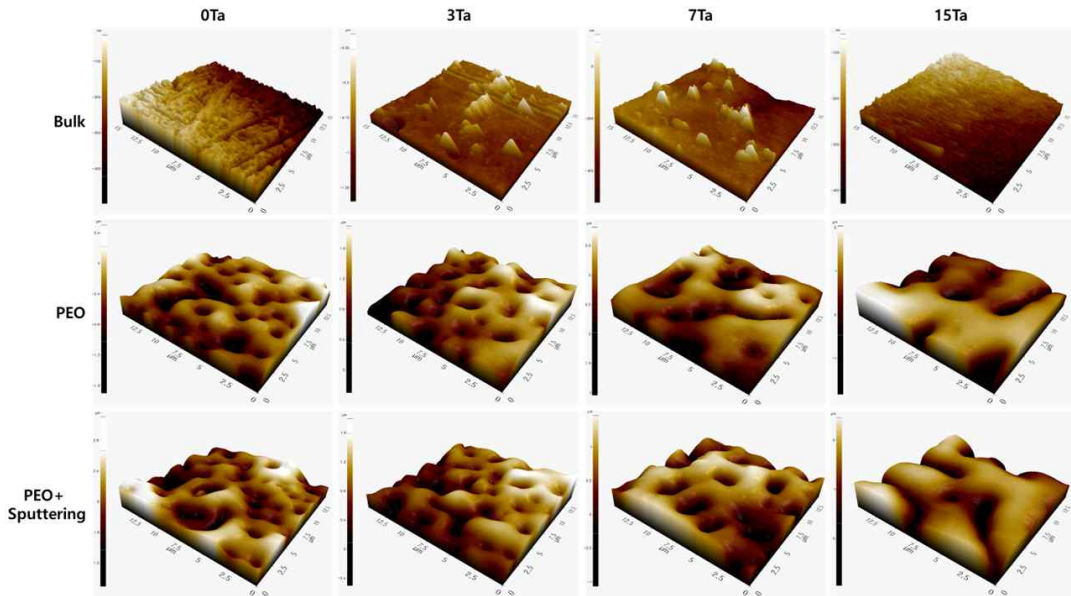
Fig. 29. AFM 3D images of Bulk, PEO, and Zr-HA coated surface on Ti-40Nb-xTa alloys.

Table 11. Surface roughness by AFM of Bulk, PEO, and Zr-HA coated surface on Ti-40Nb-xTa alloys

Surface Roughness (μm)	0Ta	3Ta	7Ta	15Ta
Bulk alloy	0.070 ± 0.031	0.089 ± 0.029	0.61 ± 0.046	0.058 ± 0.022
PEO	0.246 ± 0.017	0.311 ± 0.026	0.360 ± 0.036	0.497 ± 0.047
PEO + sputtering	0.259 ± 0.09	0.306 ± 0.020	0.376 ± 0.025	0.452 ± 0.071

Ⅳ. 5. 2. Wettability of Ti-40Nb-xTa alloys according to surface treatment method

Figure 30 shows the images of contact angle value after measuring the wettability of the HA-coated alloy surface using the static droplet method. Values of contact angle are presented in Table 11. The main factors for affecting contact angle are frequently surface roughness and chemical composition; the rougher the surface, the higher the surface energy and the smaller the contact angle [61]. First, in the case of the bulk, When Ta is added, the microstructure changes from martensite to beta structure. Therefore, when etching, the martensite structure is corroded, and the roughness of the surface is higher than that of beta structure. It can be predicted that this may appear differently depending on the type and composition of the oxide film formed on the surface as well as the roughness of the surface. The contact angle of the surface was typically lower after the PEO procedure than it was prior to surface treatment, and in a similar manner, the contact angle reduced as the Ta content increased. The contact angle of PEO + sputtering treatment was lower than that of only PEO treatment, which means that there is almost no change in roughness value. However, when HA and Zr are coated, it is thought that the contact angle is reduced because the small grainular particles on the surface affect the surface tension.
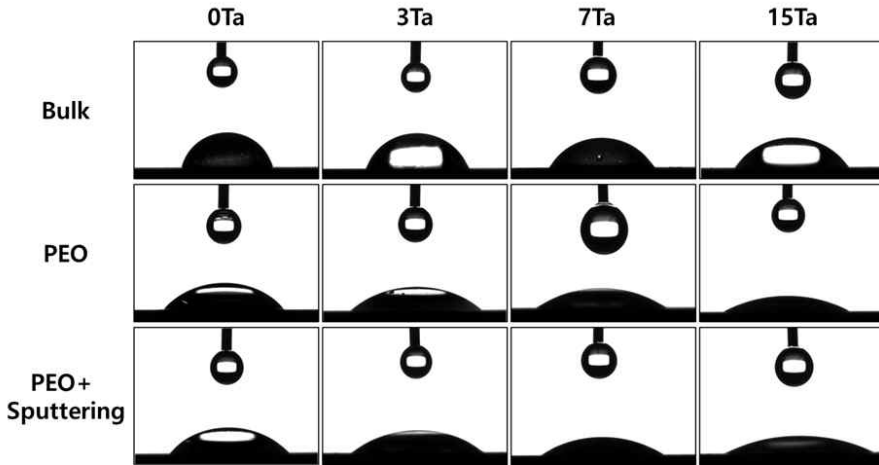
Fig. 30. Images of contact angle for Bulk, PEO, and Zr-HA coated surface on Ti-40Nb-xTa alloys.

Table 12. Contact angle of Bulk, PEO, and Zr-HA coated surface on Ti-40Nb-xTa alloys

Properties	Contact angle (˚)			
	0Ta	3Ta	7Ta	15Ta
Bulk	73.28±6.13	67.53±2.87	58.16±2.24	53.36±1.15
PEO	46.33±2.36	37.64±1.49	32.58±0.96	26.27±0.65
PEO + Sputtering	44.39±1.29	34.85±0.81	32.81±1.31	24.91±0.84

Ⅳ. 5.3. Formation and growth of hydroxyapatite (HA) in Ti-40Nb-xTa alloys in SBF solution

Figure 31 is a FE-SEM images of hydroxyapatite grown for 1 day through SBF solution on surface-treated Ti-40Nb-xTa alloys. Hydroxyapatite was observed to be nucleated over the entire surface, and growth was particularly active around the pores. Hydroxyapatite nucleated around the pores grew over time to cover the perimeter of the surface. The presence of anatase in the oxide film produced by the PEO process favors the formation of hydroxyapatite due to the crystallographic correspondence between the (110) crystal plane of anatase and the (0001) crystal plane of hydroxyapatite. This means that OH^- can combine with Ti^+ of TiO_2 to form Ti-OH in SBF solution, and the negatively charged Ti-OH$^-$ surface can selectively absorb positively charged Ca^{2+} to form calcium titanate, and as Ca^{2+} increases. It can attract PO_4^{3-} to form CaP crystals [62]. In addition, the formation of HA particles formed on the oxide film during the PEO process also helps to induce the formation of hydroxyapatite [63].

Here, the condition of affecting wettability, cell growth, and bone formation can be considered by various variables. First of all, the roughness of the surface can be considered. If the roughness of the surface increases, it is thought that the growth of the cells will be done well. When the Ta alloy element is increased in the PEO process, the roughness of the surface increases and the effect of cell growth can be obtained. In second, it can be thought that it is due to the form of the oxide film formed on the surface, and it is thought that the case where various oxide films are formed can promote the growth of cells, so the case of 15% Ta is also assumed to be advantageous. Third is the effect of HA and Zr coated on the surface. It is thought that the effect will be increased when the HA and Zr are coated, but it can be considered that the shape of the pores formed on the surface can finally grow cells well. Here, the viability of the cells was the highest in the case of 3% Ta treated with PEO, which is thought to be the effect of the well-balanced coating effect of HA and Zr on the appropriate number of pores and circular shape.
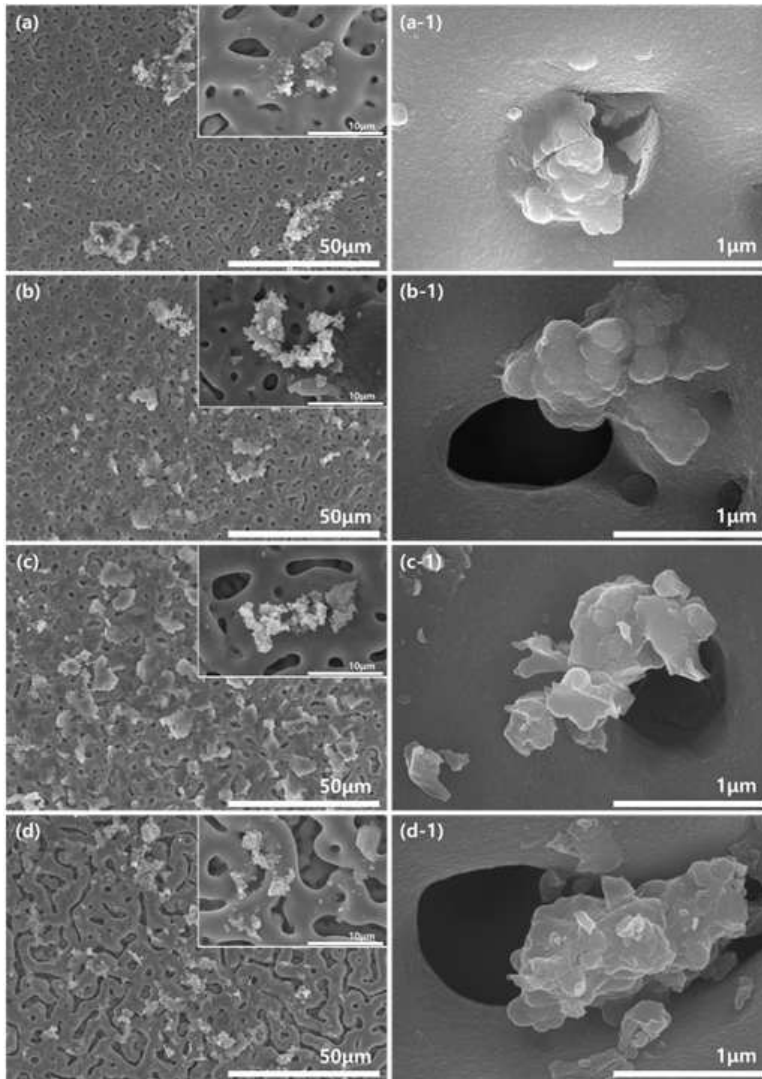
Fig. 31. FE-SEM images of HA crystal growth in SBF solution for 24 hours on the Zr-HA coated surface by RF-magnetron sputtering on PEO-treated Ti-40Nb-xTa alloys: (a) 0Ta, (a-1) high magnification of 0Ta, (b) 3Ta, (b-1) high magnification of 3Ta, (c) 7Ta, (c-1) high magnification of 7Ta, (d) 15Ta, and (d-1) high magnification of 15Ta.

Ⅴ. CONCLUSION

In this study, Ti-40Nb-xTa alloy was coated with Zr-HA through the RF-sputtering process after the PEO process. The surface properties and biocompatibility of the alloy were investigated using various methods. The conclusions are as follows.

1. As the Ta content increased in the Ti-40Nb-xTa alloy, the martensitic structure decreased. The peak of the α″ phase, which is a martensite crystal structure, mainly decreased as the Ta content increased, whereas the peak of the β phase, which is an equiaxed structure, increased. In addition, as the content of Ta increased, the indentation hardness and elastic modulus also decreased.

2. As a result of performing the PEO treatment of the Ti-40Nb-xTa alloy on the electrolytes containing Ca and P ions, the overall shape of the surface was porous, and irregularly shaped pores were observed. As the Ta content increased, the alloy surface porosity, pore size, and oxide film thickness increased, but the number of pores decreased. In addition, crystal phases of anatase, rutile, Nb_2O_5, Ta_2O_5, and HA appeared on the surface of the alloy after the PEO treatment.

3. The surface morphology of Ti-Nb-xTa alloys coated with Zr-HA through sputtering after PEO process in an electrolyte containing Ca and P ions was not different, but Zr- and HA elements were observed and detected on the surface as a result of high magnification and EDS. After the sputtering process, XRD analysis showed crystal phases of anatase, rutile, Nb_2O_5, Ta_2O_5, and HA on the surface, and additionally, Zr and HA peaks became stronger.

4. The adhesion of the Ti-Nb-xTa alloy coatings coated with PEO and Zr-HA increased as the Ta content increased in proportion to the coating thickness. In addition, when Ta increased both before and after coating, the corrosion potential increased, and

the corrosion potential after coating increased and the current density decreased due to the influence of Zr and HA, which slowed down the corrosion rate, so the corrosion resistance greatly increased.

5. After the PEO treatment, micro-sized pores were formed, resulting in a large increase in surface roughness compared to Bulk surfce. As the content of Ta increased, the pore size increased and the roughness tended to increase. The Zr-HA coating was coated in the form of a thin film, so there was no significant difference in roughness after sputtering.

6. As a result of measuring the wettability of surface-treated Ti-40Nb-xTa alloy, the contact angle of the surface-treated alloy decreased overall compared to the Bulk alloy, and the contact angle decreased in the case of increased Ta content, Zr-coating, and HA-coating on the samples.

7. Hydroxyapatite was initially nucleated as a whole on the surface of the oxide film containing anatase and HA crystal phases, and it grew mainly around the pores with precipitaion time. In addition, it is thought that Ta will have a positive effect on cell proliferation if it contains Zr and HA, which promote cell attachment and proliferation, and have good biocompatibility with the oxide film formed through surface treatment.

The Ti-40Nb-xTa alloy developed in this study is non-toxic and has a low modulus of elasticity compared to commercial Ti alloys used as implant materials. In addition, a large surface area can be obtained by forming a porous oxide film through the PEO process, and biocompatibility can be improved by doping the formed oxide film with a functional material. Therefore, it is thought that the surface-modified Ti-40Nb-xTa alloy with Zr-HA coating will shorten the healing time through rapid bone fusion between bone and implant after implant placement.

- Reference -

1. E. Zhang, X. Zhao, J. Hu, R. Wang, S. Fu, G. Qin, Antibacterial metals and alloys for potential biomedical implants, Bioact. Mater. 6 (2021) 2569-2612.

2. D.M. Brunette, P. Tengvall, M. Textor, P. Thomsen, Titanium in Medicine, Springer, New York. (2001) pp. 13‑23.

3. K.T. Kim, M.Y. Eo, T.T.H. Nguyen, S.M. Kim, General review of titanium toxicity, Int. J. Implant. Dent. 5 (2019) 10.

4. Y.H. Jeong, C.H. Lee, C.H. Chung, M.K. Son, H.C. Choe, Effects of TiN and WC coating on the fatigue characteristics of dental implant, Surf. Coat. Technol. 243 (2014) 71‑81.

5. M. Niinomi, M. Nakai, J. Hieda, Development of new metallic alloys for biomedical applications, Acta. Biomater. 8 (2012) 3888-903.

6. S. Kligman, Z. Ren, C.H. Chung, M.A. Perillo, Y.C. Chang, H. Koo, Z.Zheng, C. Li, The impact of dental implant surface modifications on osseointegration and biofilm formation, J. Clin. Med. 10 (2021) 1641.

7. M.T. Mohammed, Z.A. Khan, A.N. Siddiquee, Beta Titanium Alloys: The Lowest Elastic Modulus for Biomedical Applications: A Review, Metall. Mater. Eng. 8 (2014) 8.

8. E. Eisenbarth, D. Velten, M. Muller, R. Thull, J. Breme, Biocompatibility of β-stabilizing elements of titanium alloys, Biomaterials. 25 (2004) 5705-5713.

9. S.Y. Park, C.I. Jo, H.C. Choe, W.A. Brantley, Hydroxyapatite deposition on micropore-formed Ti-Ta-Nb alloys by plasma electrolytic oxidation for dental applications, Surf. Coat. Technol. 294 (2016) 15-20.

10. J. Izquierdo, G. Bolat, N. Cimpoesu, L. C. Trinca, D. Mareci, R. M. Souto, Electrochemical characterization of pulsed layer deposited hydroxyapatite-zirconia layers on Ti-21Nb-15Ta-6Zr alloy for biomedical application, Appl. Surf. Sci. 385 (2016) 368-378.

11. A. Fattah-alhosseini, M. Molaei, N. Attarzadeh, K.Babaei, F. Attarzadeh, On the enhanced antibacterial activity of plasma electrolytic oxidation (PEO) coatings that incorporate particles: A review, Ceram. Int. 46 (2020) 20587-20607.

12. M. Qadir, Y. Li, C. Wen, Ion-substituted calcium phosphate coatings by physical vapor deposition magnetron sputtering for biomedical applications: A review, Acta. Biomater. 89 (2019) 14-32.

13. M. Kaseem, S. Fatimah, N. Nashrah, Y.G. Ko, Recent progress in surface modification of metals coated by plasma electrolytic oxidation: principle, structure, and performance, P. Mater. Sci. 117 (2021) 100735

14. F. Songur, B. Dikici, M. Niinomi, E. Arslan, The plasma electrolytic oxidation (PEO) coatings to enhance in-vitro corrosion resistance of Ti‑29Nb‑13Ta‑4.6Zr alloys: The combined effect of duty cycle and the deposition frequency, Surf. Coat. Technol. 374 (2019) 345-354.

15. I.J. Hwang, H.C. Choe, Surface morphology and cell behavior of Zn-coated Ti-6Al-4V alloy by RF sputtering after PEO-treatment, Surf. Coat. Technol. 361 (2019) 386-395.

16. S. Durdu, O.F. Deniz, I. Kutbay, M. Usta, Characterization and formation of hydroxyapatite on Ti6Al4V coated by plasma electrolytic oxidation, J. Alloys Compd. 551 (2013) 422-429.

17. C. Capuccini, P. Torricelli, F. Sima, E. Boanini, C. Ristoscu, B. Bracci, G. Socol, M. Fini, I.N. Mihailescu, A. Bigi, Strontium-substituted hydroxyapatite coatings synthesized by pulsed-laser deposition: In vitro osteoblast and osteoclast response, Acta. Biomater. 4 (2008) 1885-93.

18. I.V. Tudose, F. Comanescu, P. Pascariu, S. Bucur, L. Rusen, F. lacomi, E. Koudoumas, M.P. Suchea, Chemical and physical methods for multifunctional nanostructured interface fabrication, Functional Nanostructured Interfaces for Environmental and Biomedical Applications. (2019) 15-26.

19. J.W. Moon, D.W. Kim, A Study on the annealed properties of ITO thin film deposited by RF-superimposed DC reactive magnetron sputtering, Kor. Inst. Surf. Eng. 40 (2007) 117-124.

20. B. Yan, J. Tan, D. Wang, J. Qiu, X. Liu, Surface alloyed Ti‑Zr layer constructed on titanium by Zr ion implantation for improving physicochemical and osteogenic properties, Prog. Nat. Sci. 30 (2020) 635-641.

21. A. Singh, P. Kuppusami, R. Thirumurugesan, R. Ramaseshan, M. Kamruddin, S.

Dash, V. Ganesan, E. Mohandas, Study of microstructure and nanomechanical properties of Zr films prepared by pulsed magnetron sputtering, Appl. Surf. Sci. 257 (2011) 9909-9914.

22. G.A Santos, The importance of metallic materials as biomaterials, Adv. Tissue. Eng. Regen. Med. Open. Access. 3 (2017) 300-302.

23. K.Y. Liu, L.X. Yin, X. Lin, S.X. Liang, Development of low elastic modulus titanium alloys as implant biomaterials, Recent. Prog. Mater. 4 (2022) 2202008.

24. Y.J. Park, Y.H. Song, J.H. An, H.J. Song, K.J. Anusavice, Cytocompatibility of pure metals and experimental binary titanium alloys for implant materials, J. Dent. 42 (2013) 1251-1258.

25. F. Habashi, Titanium, Physical and Chemical Properties, Encyclopedia of metalloproteins. (2013) 2251-2252.

26. M.R.S. Hazwani, L.X. Lim, Z. Lockman, H. Zuhailawati, Fabrication of titanium-based alloys with bioactive surface oxide layer as biomedical implants: Opportunity and challenges, Trans, Nonferrous Met. Soc. 32 (2022) 1-44.

27. A. Cunha, L. Plawinski, A. Almeida, R. Vilar, M.C. Durrieu, Multiscale femtosecond laser surface texturing of titanium and titanium alloys for dental and -orthopaedic implants, cond-mat. Universite. de. Bordeaux. (2014) 17-18.

28. S.P. Kim, H.R. Cho, H.C. Choe, Bioactive element coatings on nano-mesh formed Ti-6Al-4V alloy surface using plasma electrolytic oxidation, Surf. Coat. Technol. 406 (2021) 126649.

29. B.S. Lim, H.R. Cho, H.C. Choe, Corrosion behaviors of macro/micro/nano-scale surface modification on Ti-6Al-4V alloy for bio-implant, Thin. Solid. Films. 754 (2022) 139314.

30. M. Kaseem, H.C. Choe, Triggering the hydroxyapatite deposition on the surface of PEO-coated Ti-6Al-4V alloy via the dual incorporation of Zn and Mg ions, J. Alloys. Compd. 819 (2019) 153038.

31. M. Niinomi, Y. Liu, M. Nakai, H. Liu, H. Li, Biomedical titanium alloys with Young's moduli close to that of cortical bone, Regen. Biomater. 3 (2016) 173-85.

32. B.S. Lim, H.R. Cho, H.C. Choe, Nanotube shape changes on Ti‒6Al‒4 V alloy via various applied potential for bio‒implants, Applied. Nanoscience. 12 (2022)

3329-3336.

33. M. Kulkarni, A. Mazare, E. Gongadze, S. Perutkova, V. Kralj-lglic, I. Milosev, P. Schmuki, P. Schmuki, A. Iglic, M. Mozetic, Titanium nanostructures for biomedical applications, Nanotechnol. 26 (2015) 062002.

34. C. Prakash, S. Singh, S. Ramakrishna, G. Królczyk, C. H. Le, Microwave sintering of porous Ti‑Nb-HA composite with high strength and enhanced bioactivity for implant applications, J. Alloys. Compd. 824 (2020) 153774.

35. Y. Yang, X. Guo, Z. Dong, Effect of Nb on microstructure and mechanical properties of Ti-xNb-4Zr‑8Sn alloys, Mater. Sci. Eng. A. 825 (2021) 141741.

36. I.J. Hwang, H.C. Choe, W.A. Brantley, Electrochemical characteristics of Ti-6Al-4V after plasma electrolytic oxidation in solutions containing Ca, P, and Zn ions, Surf. Coat. Technol. 320 (2017) 458.

37. G. Adamek, M. Kozlowski, M.U. Jurczyk, P. Wirstlein, J. Zurawski, J. Jakubowicz, Formation and properties of biomedical Ti-Ta foams prepared from nanoprecursors by thermal dealloying process, Materials. 12 (2019) 2668.

38. Y.L. Zhou, M. Niinomi, T. Akahori, H. Fukui, H. Toda, Corrosion resistance and biocompatibility of Ti‑Ta alloys for biomedical applications, Mater. Sci. Eng. A. 398 (2005) 28-36.

39. L. Jue, Y. Qiumin, Y. Jian, Y. Hailin, Effects of alloying elements and annealing treatment on the microstructure and mechanical properties of Nb-Ta-Ti alloys fabricated by partial diffusion for biomedical applications, Mater. Sci. Eng. C. 110 (2020) 110542.

40. A.R. Rafieerad, M.R. Ashra, R. Mahmoodiana, A.R. Bushroa, Surface characterization and corrosion behavior of calcium phosphate-base composite layer on titanium and its alloys via plasma electrolytic oxidation: A review paper, Mater. Sci. Eng. C. 57 (2015), 397-413.

41. J.I. Kang, M.K. Son, H.C. Choe, A.B. William, Bone-like apatite formation on manganese-hydroxyapatite coating formed on Ti-6Al-4V alloy by plasma electrolytic oxidation, Thin Solid Films. 620 (2016) 126-131.

42. Y.H. Jeong, H.C. Choe, Y.M. Ko, Electrochemical properties of Ti-30Ta-(3 ~ 15)Nb alloys coated by HA/Ti compound layer, J. Kor. Inst. Surf. Eng. 41 (2008)

57-62.

43. K. Srinivasan, L1(0) iron-platinum on nanocrystalline HITPERM soft magnetic underlayers for perpendicular recording media, Carnegie Mellon University, United States. (2004) 3141087.

44. N. Nagisa, T. Nakano, N. Hashiguchi, W. Fujitani, Y. Umakoshi, M. Shimahara, Analysis of biological apatite orientation in rat mandibles, Oral. Sci. Inter. 7 (2010) 19-25.

45. E. Boanini, M. Gazzano, A. Bigi, Ionic substitutions in calcium phosphates synthesized at low temperature, Acta. Biomater. 6 (2010) 1882-1894.

46. A. Cadi-Essadek, A. Roldan, N.H.D. Leeuw, Density functional theory study of the interaction of H_2O, CO_2 and CO with the ZrO_2 (111), Ni/ZrO_2 (111), YSZ (111) and Ni/YSZ (111) surfaces, Surf. Sci. 653 (2016) 153-162.

47. F. Mussano, T. Genova, S. Guastella, M.G. Faga, S. Carossa, Possible role of microcrystallinity on surface properties of titanium surfaces for biomedical application, Crystalline and Non-crystalline Solids. (2016) 17-35.

48. P. Wilson, Recent developments in the study of recrystallization, University of Tsukuba, Japan. (2013) 117-138.

49. Y.H. Jeong, I.B. Son, H.C. Choe, Formation of surface roughness on the Ti-35Nb-xZr alloy using femtosecond laser for biocompatibility, Procedia. Eng. 10 (2011) 2393-2398.

50. O.A. Waseem, K.B. Woller, Evolution in microstructure and hardness of titanium‐zirconium‐molybdenum (TZM) alloy after depth marker implantation for erosion diagnostic in fusion devices, Mater. Chem. Phys. 258 (2021) 123883.

51. S.A. Souzaa, R.B. Manicardi, P.L. Ferrandini, C.R.M. Afonso, A.J. Ramirez, R. Caram, Effect of the addition of Ta on microstructure and properties of Ti‐Nb alloys, J. Alloys. Compd. 5004 (2010) 330-340.

52. R. Chaharmahali, A. Fattah-alhosseini, K. Babaei, Surface characterization and corrosion behavior of calcium phosphate (Ca-P) base composite layer on Mg and its alloys using plasma electrolytic oxidation (PEO): A review, J. Magnes. Alloy. 10 (2020) 1-20.

53. A. Fattah-alhosseini, R. Chaharmahali, K. Babaei, Effect of particles addition to

solution of plasma electrolytic oxidation (PEO) on the properties of PEO coatings formed on magnesium and its alloys: A review, J. Magnes. Alloy. 8 (2020) 799-818.

54. T. Mi, B. Jiang, Z. Liu, L. Fan, Plasma formation mechanism of microarc oxidation, Electrochim. Acta. 123 (2014) 369-977.

55. S. Panda, C.K. Biswas, S. Paul, A comprehensive review on the preparation and application of calcium hydroxyapatite: a special focus on atomic doping methods for bone tissue engineering, Ceram. Int. 47 (2021) 28122-28144.

56. W. Yi, Y. Huijun. C. Chuanzhong. Z. Zhihuan, Review of the biocompatibility of micro-arc oxidation coated titanium alloys, Materials & Design. 85 (2015) 640-652.

57. A.L. da Silvaa, D.N.F. Muche, S. Dey, D. Hotza, R.H.R. Castro, Photocatalytic Nb_2O_5-doped TiO_2 nanoparticles for glazed ceramic tiles, Ceram. Int. 42 (2016) 5113-5122.

58. M.G. Park, H.C. Choe, Corrosion behaviors of bioactive element coatings on PEO-treated Ti-6Al-4V alloys, Surf. Coat. Tech. 376 (2019) 44‑51.

59. M.A.F. Martinez, I.F. Balderrama, P.S.B.H. Karam, R.C. Oliveira, F.A. Oliveira, C.R. Grandini, F.B. Vicente, A. Stavropoulos, M.S.R. Zangrando, A.C.P. Santana, Surface roughness of titanium disks influences the adhesion, proliferation and differentiation of osteogenic properties derived from human, Int. J. Implant. Dent. 6 (2020) 46.

60. H.H. Huan, C.T. Ho, T.H. Lee, T.L. Lee, K.K. Liao, F.L. Chen, Effect of surface roughness of ground titanium on initial cell adhesion, Biomol. Eng. 21 (2004) 93-97.

61. H.R. Cho, H.C. Choe, Morphology of hydroxyapatite and Sr coatings deposited using radio frequency-magnetron sputtering method on nanotube formed Ti-6Al-4V alloy, Thin. Solid. Films. 735 (2021) 138893.

62. J. Weng, Q. Liu, J.G.C. Wolke, D. Zhang, K.D. Groot, The role of amorphous phase in nucleating bone-like apatite on plasma sprayed hydroxyapatite coatings in simulated body fluid, J. Mater. Lett. 16 (1997) 335-337.

63. M. Kassem, H.C. Choe, Electrochemical and bioactive characteristics of the porous surface formed on Ti-xNb alloys via plasma electrolytic oxidation, Surf. Coat.

Technol. 378 (2019) 125027.